A systematic look at the effects of radiative feedback on disc galaxy formation

Roskar, R ; Teyssier, R ; Agertz, O ; Wetzstein, M ; Moore, B

Abstract: Galaxy formation models and simulations rely on various feedback mechanisms to reproduce the observed baryonic scaling relations and galaxy morphologies. Although dwarf galaxy and giant elliptical properties can be explained using feedback from supernova and active galactic nuclei, Milky Way-sized galaxies still represent a challenge to current theories of galaxy formation. In this paper, we explore the possible role of feedback from stellar radiation in regulating the main properties of disc galaxies such as our own Milky Way. We have performed a suite of cosmological simulations of the same ˜1012 M halo selected based on its rather typical mass accretion history. We have implemented radiative feedback from young stars using a crude model of radiative transfer for ultraviolet and infrared radiation. However, the model is realistic enough such that the dust opacity plays a direct role in regulating the efficiency of our feedback mechanism. We have explored various models for the dust opacity, assuming different constant dust temperatures, as well as a varying dust temperature model. We find that while strong radiative feedback appears as a viable mechanism to regulate the stellar mass fraction in massive galaxies, it also prevents the formation of discs with reasonable morphologies. In models with strong stellar radiation feedback, stellar discs are systematically too thick while the gas disc morphology is completely destroyed due to the efficient mixing between the feedback-affected gas and its surroundings. At the resolution of our simulation suite, we find it impossible to preserve spiral disc morphology while at the same time expelling enough baryons to satisfy the abundance matching constraints.

DOI: https://doi.org/10.1093/mnras/stu1548

Monthly Notices
of the
ROYAL ASTRONOMICAL SOCIETY

MNRAS **444,** 2837–2853 (2014) doi:10.1093/mnras/stu1548

A systematic look at the effects of radiative feedback on disc galaxy formation

Rok Roškar,[1]★ Romain Teyssier,[1] Oscar Agertz,[2,3,4] Markus Wetzstein[1] and Ben Moore[1]

[1]*Institute for Computational Science, University of Zürich, Winterthurerstrasse 190, CH-8057 Zürich, Switzerland*
[2]*Department of Physics, University of Surrey, Guildford, GU2 7XH Surrey, UK*
[3]*Kavli Institute for Cosmological Physics and Enrico Fermi Institute, The University of Chicago, Chicago, IL 60637, USA*
[4]*Department of Astronomy & Astrophysics, The University of Chicago, Chicago, IL 60637, USA*

Accepted 2014 July 30. Received 2014 July 30; in original form 2013 August 27

ABSTRACT

Galaxy formation models and simulations rely on various feedback mechanisms to reproduce the observed baryonic scaling relations and galaxy morphologies. Although dwarf galaxy and giant elliptical properties can be explained using feedback from supernova and active galactic nuclei, Milky Way-sized galaxies still represent a challenge to current theories of galaxy formation. In this paper, we explore the possible role of feedback from stellar radiation in regulating the main properties of disc galaxies such as our own Milky Way. We have performed a suite of cosmological simulations of the same $\sim 10^{12}\,\mathrm{M}_{\odot}$ halo selected based on its rather typical mass accretion history. We have implemented radiative feedback from young stars using a crude model of radiative transfer for ultraviolet and infrared radiation. However, the model is realistic enough such that the dust opacity plays a direct role in regulating the efficiency of our feedback mechanism. We have explored various models for the dust opacity, assuming different constant dust temperatures, as well as a varying dust temperature model. We find that while strong radiative feedback appears as a viable mechanism to regulate the stellar mass fraction in massive galaxies, it also prevents the formation of discs with reasonable morphologies. In models with strong stellar radiation feedback, stellar discs are systematically too thick while the gas disc morphology is completely destroyed due to the efficient mixing between the feedback-affected gas and its surroundings. At the resolution of our simulation suite, we find it impossible to preserve spiral disc morphology while at the same time expelling enough baryons to satisfy the abundance matching constraints.

Key words: galaxies: evolution – galaxies: formation – galaxies: spiral – galaxies: structure.

1 INTRODUCTION

The formation of disc galaxies like the Milky Way (MW) is an outstanding research problem of modern astrophysics. On large scales, the Lambda-CDM paradigm provides a framework for the formation of structure that reproduces observed properties remarkably well (Springel, Frenk & White 2006). On small scales, however, the gravity-only evolution diverges sharply from observed properties such as the satellite luminosity function (Moore et al. 1999) and the inclusion of baryonic physics becomes important. In fully cosmological simulations of MW-mass galaxies, various stages of success in meeting observational constraints have been reported in the literature since the 1990s (e.g. Steinmetz & Muller 1995; Navarro & Steinmetz 1997; Abadi et al. 2003; Governato et al. 2007; Agertz, Teyssier & Moore 2011; Guedes et al. 2011). For a number of years, two serious issues needed resolution. The first of these, the 'overcooling problem' is a consequence of short cooling time-scales in the dense protogalactic fragments early in the process of galaxy formation. This leads to rapid conversion of gas into stars and locking up the baryons in the low angular momentum components, thus preventing the formation of extended structures at lower redshifts (White & Rees 1978; Navarro & White 1994). The second issue is the 'angular momentum catastrophe', which occurs due to the loss of angular momentum during the merging process. The fragments entering the main halo lose their angular momentum due to dynamical friction, resulting in small discs with peaked rotation curves (Navarro & White 1994).

Both of these problems can be overcome to some extent by increased mass and spatial resolution and by considering the effects

★ E-mail: roskar@physik.uzh.ch

of various feedback processes on the gas to prevent early conversion of baryons into stars. Still, until recently many simulations were plagued by 'peaky' rotation curves, signifying that the concentrations of baryons are still too high in the central parts, even if they form relatively extended discs (e.g. Governato et al. 2007). In the past, many simulations of massive spirals typically fell below the Tully–Fischer (Tully & Fisher 1977) relation due to high central mass concentrations and radially declining rotation curves (Navarro & Steinmetz 2000; Abadi et al. 2003; Governato et al. 2004), though with careful comparisons between model and observational measurements relatively good agreement is now claimed by many groups. In particular, the choices of subgrid parameters and simulation resolution in the *Eris* simulation (Guedes et al. 2011) seem to work in all of these respects, resulting in a MW-like disc galaxy with a flat rotation curve that satisfies most of the observational scaling relations.

The abundance of baryons with low angular momentum can be traced to the efficient early condensation of gas and subsequent star formation (SF; Brook et al. 2011). Stars that form near the centres of their host haloes will remain at the centres of potential wells throughout the merging process; therefore, forming stars early effectively ensures a large amount of mass to be locked up in low angular momentum material. Boosting the effect of supernova (SN) feedback by increasing its coupling efficiency slows down the collapse of gas clouds and raising the threshold for SF modulates early SF and helps preserve the angular momentum of baryons until late times. This technique requires sufficient resolution to 'resolve' the star-forming clumps, and has therefore proven particularly successful in models of dwarf galaxies (Governato et al. 2010), where modest numbers of particles yield sufficiently high mass resolution. Strong feedback has also been suggested as a mechanism capable of resolving the problem of cusp formation in collisionless Lambda-CDM simulations (e.g. Pontzen & Governato 2012).

A further indication that the conversion of gas into stars is too efficient in current state-of-the-art simulations of galaxy formation is the overabundance of stars at fixed halo mass compared to observationally derived stellar-mass-halo-mass (SMHM) relation from e.g. Conroy & Wechsler (2009), Moster et al. (2010). However, unlike the issues related to angular momentum, 'conventional' stellar feedback, i.e. injection of thermal energy corresponding to SN explosions, has proven unsuccessful in curbing this problem completely. Recently, it has been shown that radiation from young stars in star-forming regions may play a more important role in regulating SF than SN explosions. Ultraviolet (UV) radiation, converted into far-infrared radiation by dust grains, can provide enough momentum to the surrounding gas to dissolve giant molecular clouds (GMCs) on significantly shorter time-scales than required by SN feedback alone (Murray, Quataert & Thompson 2010). Further, such radiation pressure can form cold gas outflows at the escape velocity of the host halo (Murray, Ménard & Thompson 2011). Implementations of this process in several hydrodynamic codes have shown that it is a promising avenue for halting SF and sufficiently enriching the surrounding intergalactic medium (IGM; Hopkins, Quataert & Murray 2011; Brook et al. 2012; Stinson et al. 2012; Wise et al. 2012; Agertz et al. 2013; Stinson et al. 2013b). However, while stopping the formation of a bulge in its entirety and suppressing the stellar mass fraction is natural in such models, it appears more difficult to at the same time form an extended *thin* disc exhibiting the usual structure such as spiral arms.

In this paper, we report on our efforts to further explore the effects of stellar radiative feedback on the properties of the resulting MW-like disc galaxies. We implement stellar radiation feedback in the adaptive mesh refinement (AMR) hydrodynamic code RAMSES and perform a suite of simulations of the same cosmological initial conditions with varying feedback prescriptions. Our paper is organized as follows: in Section 2, we briefly describe the simulation code followed by a detailed description of the different implementations of SN feedback in Section 2.6 and stellar radiative feedback in Section 3; in Section 4, we describe the results of our simulations; in Section 5, we discuss the caveats inherent in our modelling approach; we briefly discuss our main results and summarize in Section 6.

2 METHODS

In this section, we describe our methodology to model a disc galaxy in a cosmological context with the AMR code RAMSES. We first describe our initial conditions, selected from a set of dark matter only (DMO) simulations. This required us to define and extract a high-resolution region containing only low-mass dark matter particles and gas cells that will end up in our final halo at redshift 0. We then describe briefly our numerical methods to model gas dynamics, gas cooling and heating processes, SF and supernovae (SNe) feedback. Our implementation of radiative transfer and the associated radiative feedback from stellar radiation is discussed in detail in Section 3.

The vast majority of the analysis presented in this paper was done using the PYTHON-based simulation analysis framework PYNBODY[1] (Pontzen et al. 2013) in the IPYTHON environment (Pérez & Granger 2007). Halo centres were identified with the HOP halo finder (Eisenstein & Hut 1998) and further substructure analysis was performed with the Amiga Halo Finder (Knollmann & Knebe 2009). All units are physical unless otherwise stated.

2.1 Initial conditions for zoom-in cosmological simulations

The cosmological parameters used in this study are $H_0 = 70.4$ km s^{-1} Mpc^{-1}, $\Omega_\mathrm{m} = 0.272$, $\Omega_\Lambda = 0.728$, $\Omega_\mathrm{b} = 0.045$. We first performed a DMO simulation in a periodic 200 Mpc comoving box. The simulation used $N_\mathrm{d} = 512^3$ particles, a minimum level of refinement $\ell_\mathrm{min} = 9$ and a maximum level $\ell_\mathrm{max} = 14$ and was run down to redshift zero. The particle mass for this low-resolution simulation was $m_\mathrm{p} = 2.2 \times 10^9$ M$_\odot$. We then identified a MW halo candidate with mass[2] $M_{200} = 6 \times 10^{11}$ M$_\odot$ with a rather typical merger and mass accretion history and free of any neighbours more massive than half its mass. We then selected a spherical region of radius $3 \times R_{200}$ around the halo centre, and traced the particles in this region back to their original position in the initial conditions, at a redshift $z_\mathrm{ini} = 100$. The Lagrangian volume defined by these particles was resampled to much higher resolution, with an effective resolution in the halo Lagrangian volume of 8192^3, corresponding to a dark particle mass of $m_\mathrm{p} = 4.5 \times 10^5$ M$_\odot$ and an initial baryonic mass in each high-resolution gas cell of $m_\mathrm{b} = 8.9 \times 10^4$ M$_\odot$. Particles and gas cells of increasingly coarser resolutions were carefully positioned around the high-resolution region, so that a buffer zone of at least 10 cells is sampling each level before moving to the next. This strategy allowed us to sample the final halo with $N_{200c} = 1.4 \times 10^6$ dark matter particles, for a total number of high- and low-resolution dark matter particles of $N_\mathrm{d} = 7.1 \times 10^6$.

[1] http://pynbody.github.io

[2] M_{200} is the mass inside R_{200}, which is defined as the radius where the mean density $\bar{\rho} = 200 \times \rho_\mathrm{crit} = 200 \times (3H^2)/(8\pi G)$.

In our final halo, the mass fraction due to low-resolution particles is 2.6×10^{-4}, demonstrating that our halo suffered from negligible contamination. This corresponds to 46 low-resolution particles that have penetrated the outskirts of our main halo, due to a grazing interaction with a nearby, poorly resolved satellite halo.

2.2 Adaptive mesh refinement

Although the mesh is already refined in the initial conditions, to define the high-resolution region and the coarser particles and cells around it, we trigger additional refinements based on the so-called quasi-Lagrangian strategy. Cells are subdivided in eight new children cells if the dark matter mass exceeds $8 \times m_{\rm d}$ or if the total baryonic mass (gas plus stars) exceeds $8 \times m_{\rm b}$. Since we want additional refinements to be restricted to the high-resolution region, we use only high-resolution particles to compute the dark matter mass that triggers refinements. For baryons, we use a scalar field (a colour function) that takes the value 1 in the high-resolution region and 0 outside, and that is passively advected by the flow. The baryonic mass contained in each cell can trigger refinement only if the colour function is above a threshold set to 1 per cent. In simulations where gas is allowed to cool, nothing can prevent baryons from collapsing into arbitrarily small clumps. Although DMO only simulations maintain a quasi-fixed physical resolution, owing to the 'stable clustering' property of dark matter non-linear dynamics, we need to enforce this behaviour for the gas. Our strategy is to release additional refinement levels at pre-determined epochs, so that the effective physical resolution remains almost constant. In practice, we release levels $\ell = (17, 18, 19, 20)$ at expansion factors $a = (0.1, 0.2, 0.4, 0.8)$. In other words, the spatial resolution is kept almost fixed (within a factor of 2), to a minimum value of $\Delta x_{\rm min} = 160$ pc from redshift 9 down to redshift 0. Before redshift 9, our spatial resolution is kept fixed in comoving units, allowing refinement up to $\ell = 16$. The maximum level of refinement $\ell_{\rm max} = 20$ was conservatively determined by running first a reference DMO simulation at the same mass resolution, and observing which maximum level of refinement was actually opened during the course of the halo formation. In this way, we know for sure that our main halo will not be affected by two-body relaxation effects, since $\ell_{\rm max} = 20$ is precisely the spatial resolution it would have reached naturally without baryonic physics.

2.3 Gas and dark matter dynamics

Dark matter is modelled using the standard Adaptive Particle Mesh method (Kravtsov, Klypin & Khokhlov 1997; Teyssier 2002). The Poisson equation is solved on each level using the multigrid scheme with Dirichlet boundary conditions on arbitrary domains (Guillet & Teyssier 2011). Gas dynamics is modelled by solving the Euler equations with a second-order unsplit Godunov scheme based on the MUSCL method (Teyssier 2002). We used the HLLC Riemann solver and the MinMod slope limiter (see Fromang, Hennebelle & Teyssier 2006, for details).

One key aspect of self-gravitating fluids simulations is to be able to resolve spatially the Jeans length, as well as the Jeans mass (Truelove et al. 1997). We use the now standard technique of the 'polytropic pressure floor'. The idea is to define the total gas pressure as the sum of the thermal pressure and an artificial polytropic pressure $P_{\rm J}$, noted here with index J since it refers to the Jeans length. This polytropic pressure floor is computed so that the Jeans length is always larger than or equal to four cells:

$$P_{\rm J} = (4\Delta x_{\rm min})^2 \frac{G}{\pi\gamma}\rho^2. \quad (1)$$

When gas cooling is very effective, the thermal pressure can fall below the polytropic pressure floor. In this case, we have reached the minimum temperature (and the associated maximum density) beyond which our limited resolution cannot properly follow the thermal and dynamical state of the gas. Using standard cooling recipes, the equilibrium gas temperature as solar metallicity can be roughly approximated by (Bournaud et al. 2010; Teyssier, Chapon & Bournaud 2010)

$$T_{\rm eq} \simeq \frac{5000}{\sqrt{n_{\rm H}({\rm H\,cm^{-3}})}}\ {\rm K}. \quad (2)$$

Equating the two previous pressure $P_{\rm eq}(\rho) = P_{\rm J}(\rho)$ gives us the maximum density $\rho_{\rm J}$ and the minimum temperature $T_{\rm J}$ one can reach reliably during the course of the simulation, given the adopted spatial resolution $\Delta x_{\rm min}$. In our case, our physical resolution is $\Delta x_{\rm min} = 160$ pc, so we have $\rho_{\rm J} \simeq 2.4$ H cm^{-3} and $T_{\rm J} \simeq 3200$ K.

2.4 Gas cooling and heating

Gas thermodynamics is modelled using an optically thin cooling and heating function. Hydrogen and helium chemistry is solved assuming photoionization equilibrium (Katz, Weinberg & Hernquist 1996). Metal cooling at both high and low temperatures (infrared hyperfine line cooling) is also included, using a simple model for the effect of photoionization. A uniform UV radiation background is considered and turned on at a reionization redshift $z_{\rm reion} = 8.5$ (Haardt & Madau 1996). We have also implemented a simple model for self-shielding, so that high-density gas suppresses the local UV flux as

$$F_{\rm UV} = F_{\rm UV,0} \exp\left[-\left(\frac{n_{\rm H}}{0.01\ {\rm H\,cm^{-3}}}\right)\right]. \quad (3)$$

The local cooling and heating rates are adjusted accordingly. Note that we entirely neglect radiation from nearby young stars in the cooling and heating curves. It will be introduced later in our feedback model.

2.5 SF model

We model SF using a Schmidt law, where the local star formation rate (SFR) is computed as

$$\dot{\rho}_\star = \epsilon_* \frac{\rho_{\rm gas}}{t_{\rm ff}} \quad \text{for} \quad \rho_{\rm gas} > \rho_*. \quad (4)$$

The SF density threshold is chosen to be equal to the maximum resolvable density $\rho_* = \rho_{\rm J} = 2.4$ H cm^{-3}. The local star formation efficiency (SFE) is set to $\epsilon_* = 0.01$, a low value suggested by observations of nearby molecular clouds (Krumholz & Tan 2007) and consistent with the Kennicutt relation (Agertz et al. 2011). Stellar particles are created using the stochastic model presented in Rasera & Teyssier (2006). We choose the stellar particle mass m_* to be exactly equal to the baryonic mass resolution $m_{\rm b}$. We then draw a Poisson random process with Poisson parameter $\lambda = \rho_* \Delta x^3 \Delta t / m_*$ to spawn individual star particles at the required rate, where Δt is the simulation time step.

2.6 SNe feedback

We model SNe feedback as a direct energy injection into gas cells containing stellar particles older than 10 Myr. Injecting this energy in pure thermal form would result in a strong dilution of the SNe energy and its immediate cooling thereafter. We use instead the implementation presented in Teyssier et al. (2013): we inject the SNe energy in a non-thermal energy component, that could be interpreted as unresolved turbulence, or an additional relativistic, magnetized fluid, such as cosmic rays. Independently of the exact underlying process, we assume that this non-thermal component's energy decays at a fixed dissipation rate defined by $t_{\rm diss} = 10$ Myr. Cells with a non-thermal energy component larger than the thermal energy have their cooling shut off temporarily, mimicking a popular technique used in SPH (smoothed particle hydrodynamics) codes (e.g. Stinson et al. 2006, see Teyssier et al. 2013 for more details). This model was used successfully to follow the evolution of a high-resolution isolated dwarf galaxy (Teyssier et al. 2013). We are applying it here for the first time for a MW-sized halo in a cosmological zoom-in simulation. In order to maximize the effect of SNe feedback, we have also assumed that the initial mass function (IMF) is the one given by Chabrier (2001), which corresponds to 20 per cent of the mass of a single stellar population (SSP) going SNe. A Salpeter IMF would have given only 10 per cent.

A major caveat of cosmological simulations at resolution of the order of 100 pc and above is that the vertical thickness of the disc, as well as individual molecular clouds, are poorly resolved. SF will therefore generate an artificially smooth distribution of young stars, and any feedback those stars may provide to the interstellar medium (ISM) will be similarly smoothly distributed. Following ideas discussed recently in the literature (Dalla Vecchia & Schaye 2012; Agertz et al. 2013), we have decided to implement a stochastic model of exploding clouds. The idea is to first choose a fixed, typical GMC mass, here $M_{\rm GMC} = 2 \times 10^6\,{\rm M}_\odot$. This is obviously a free parameter, and we have chosen this value, because it is close to the characteristic mass of GMCs in the Galaxy (Krumholz, McKee & Tumlinson 2009). We then draw a random number x from a uniform distribution between 0 and 1. The mass of the stellar particle being m_*, we require x to be lower than $m_*/M_{\rm GMC}$ to trigger a SN event. The energy of this now much rarer event is multiplied by the factor $M_{\rm GMC}/m_*$ so that the total SN energy is statistically conserved. Using this stochastic model, we now have single explosion events that are close to the energy released by individual GMCs in a disc galaxy. Note that this model would have been unnecessary for a higher resolution (better than $\sim$1pc) simulation, since in this case we would have resolved individual GMCs.

Note that the specific choice we made for $M_{\rm GMC}$ is important, since it fixes the typical energy scale of exploding SNe bubble. In our highest resolution run, for which the particle and gas cell masses were reduced by a factor of 8, we have kept the same value of $M_{\rm GMC} = 2 \times 10^6\,{\rm M}_\odot$, to make sure that this energy scale remains the same. We believe that this parameter should be set to the typical mass of the largest GMC expected in our simulated disc. The caveat here is that this mass scale is likely to vary with redshift, as high-redshift discs are more gas rich and have larger clump sizes. A larger clump mass will result into fewer more energetic events, while a smaller value would give more frequent, but weaker explosions. Since, in this context, it is critical to accelerate the gas up to the Galaxy escape velocity, choosing a large enough mass will make feedback stronger. On the other hand, if $M_{\rm GMC}$ is too large, we might create isolated, devastating events, which are unrealistic, since they would correspond to unrealistically large GMC. With these caveats in mind, we consider that $M_{\rm GMC} = 2 \times 10^6$ will maximize the effect of SN feedback, while remaining within realistic energy ranges for typical galactic super bubbles. Keeping this mass constant, while increasing the resolution even more than what we do here, might result in increasing the gas temperature so much that one no longer needs to shut down radiative cooling (Dalla Vecchia & Schaye 2012).

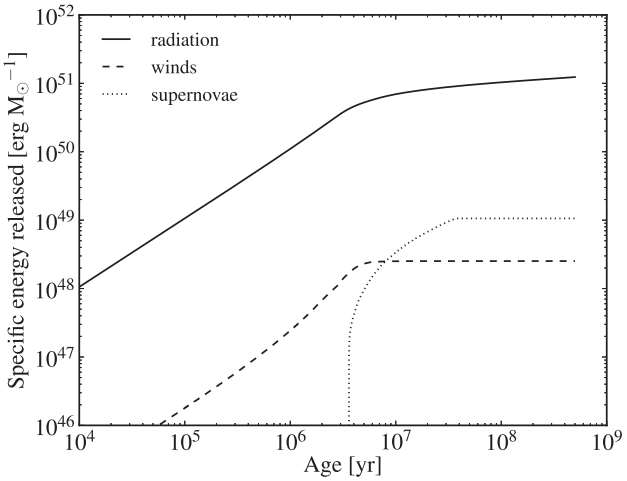

Figure 1. Comparison of contributions to the cumulative feedback energy budget from stellar radiation, winds, and SN Type II explosions for a SSP calculated using STARBURST99. The energy available through radiation of massive stars is a factor of $\sim$100 larger than the combined energy of winds and SNe.

The total energy released by a SSP is well known from stellar evolution models. We show in Fig. 1 the cumulative energy released per unit solar mass of a SSP, using the model STARBURST99 (Leitherer et al. 1999). The energy release is divided into contributions from radiation (coming mainly from massive stars), stellar winds, injected into the surrounding gas right after the first stars have formed and SNe Type II (SNII), which contribute only after 3 Myr (and mostly around 10 Myr). From Fig. 1, it is clear that the energy released in form of radiation is 100 times larger than the energy released in both SNe and winds. Formulated differently: a SSP of 100 M$_\odot$ will host only one 10 M$_\odot$ massive star progenitor that will release 10^{51} erg as it goes SN. The same SSP would have already injected 10^{53} erg of energy in the form of (mostly) UV radiation into its environment. This shows that stellar radiation energy, *if one manages to absorb it efficiently into the ISM*, is much more abundant than SNe and wind energy. This is precisely the reason why radiative feedback appears as an appealing mechanism to regulate the SFE in massive galaxies (e.g. Murray et al. 2011).

3 RADIATION FEEDBACK

In this section, we describe the various ingredients we use to model the effect of stellar radiation on the surrounding gas. We first provide analytical arguments to justify the need for radiative feedback from young massive stars in large galaxies such as the MW. This simple derivation will be useful to interpret the numerical results we present in the rest of the paper. We then describe in great detail our numerical implementation of infrared (IR) radiation transfer on dust grains. We then compare our implementation to other recent works studying the effect of radiation feedback on galaxy formation.

3.1 A simple analytical model for feedback

We consider a typical star-forming molecular cloud of total mass $M_{\rm cl}$. SF in the cloud proceeds inefficiently so that the final mass fraction in stars is of the order of $f_* \simeq 0.1$. Note that this parameter is different than our SFE parameter ϵ_*: it would be possible to convert 100 per cent of the cloud mass into stars with a low SFE if the cloud lifetime is much longer than the local free-fall time. On the other hand, the so-called infant mortality of star clusters observed in nearby star bursting galaxies suggest that an upper limit for the final mass fraction in stars is $f_* < 0.3$, otherwise most star clusters would survive the disruption of their parent molecular clouds, in contradiction with observations (Bastian & Goodwin 2006).

We now consider that SNe are responsible for disrupting the parent molecular cloud. We can compute the total energy released by SNII explosions as

$$E_{\rm SN} = \eta_{\rm SN} f_* M_{\rm cl} \epsilon_{\rm SN}, \quad (5)$$

where $\eta_{\rm SN}$ is the mass fraction of the stellar population going SNe (0.1 for Salpeter and 0.2 for Chabrier IMF) and $\epsilon_{\rm SN} \simeq 10^{50}$ erg $\mathrm{M}_\odot^{-1}$ is the specific energy released by each SN, normalized over the entire stellar population. For the purposes of this simplified calculation, we assume that the SNe energy is released at the centre of the cloud in one single giant explosion, and that the dynamics of the blast wave is entirely non-dissipative. Using the Sedov self-similar solution of a point explosion, we can compute the velocity of the blast wave as it reaches the edge of our spherical cloud:

$$v_{\rm Sedov} = \frac{2}{5}\sqrt{\frac{E_{\rm SN}}{M_{\rm cl}}} \simeq 90\sqrt{\frac{\eta_{\rm SN}}{0.1}}\sqrt{\frac{f_*}{0.1}}\ \mathrm{km\,s^{-1}}, \quad (6)$$

which does not depend on the cloud size. Pushing the only two parameters to their upper limits ($\eta_{\rm SN} = 0.2$ for a Chabrier IMF and $f_* = 0.3$ for a marginally bound star cluster), we obtain a maximum explosion velocity $v_{\rm Sedov} \simeq 220\ \mathrm{km\,s^{-1}}$. The star-forming cloud will become unbound in this non-dissipative scenario (for reasonable values of the cloud binding energy), but the velocity of the cloud remnants will not be larger than the escape velocity of a MW-like galaxy.

The escape velocity at the centre of a NFW halo is $v_{\rm esc} \simeq 2 \times V_{\rm max} \simeq \sqrt{c}V_{200}$ (Navarro, Frenk & White 1997), where $c \simeq 10$ is the halo concentration parameter and $V_{200} \simeq 220\ \mathrm{km\,s^{-1}}$ is the circular velocity of the MW halo. This leads to $v_{\rm esc} \simeq 700\ \mathrm{km\,s^{-1}}$, much larger than our most optimistic cloud explosion velocity. At high redshift, the circular velocity increases as $\sqrt{1+z}$ for a fixed halo mass, making the situation even more difficult. Moreover, it is often considered that large spiral galaxies have a rather quiescent merger history, so that the halo mass is probably mostly in place before redshift 2, closing the window for efficient SNe-driven feedback very early on. Finally, since SNe blast waves are probably dissipative (during the 'snow plow' phase) before they reach the edge of their parent clouds, a more realistic estimate of the momentum acquired by the cloud will be even lower for SNe feedback in giant galaxies such as the MW.

This discussion suggests that SNe feedback alone cannot regulate the baryonic content in galaxy discs and therefore affect the overall SFE. Radiative feedback, on the other hand, provides a viable mechanism to launch very fast winds and eject a significant fraction of baryons out of the disc. In the previous equations, multiplying $\epsilon_{\rm SN}$ by a factor of 100 (as suggested by Fig. 1) increases the cloud explosion velocity from 90 to 900 $\mathrm{km\,s^{-1}}$, which is comfortably above the escape velocity. The only conditions for radiative feedback to be efficient are that: (1) the cloud must be sufficiently opaque to IR radiation so that the available energy is absorbed by the cloud and not radiated away, and (2) the absorbed radiation energy is transformed into gas momentum, most probably by radiation-pressure effects. We model and test the first condition in a realistic cosmological setting in Section 4 using the radiation transfer model presented in Section 3.2 below. We assume that the absorbed radiation energy is maximally transferred into the gas momentum, using our non-thermal energy scheme resulting in a long, non-dissipative period 10 Myr after the SNe+radiation energy has been released. Testing the second condition in a realistic cosmological environment would require radiative transfer calculations which are beyond the scope of this paper.

The above analytical estimates are also interesting because they are close to our numerical implementation of radiative feedback described in detail in Section 3.2 below. We use a rather long (10 Myr) dissipation time-scale for our non-thermal energy, which is close to the previous adiabatic blast wave model. We would like to compare how this analytical blast wave model compares to other radiative feedback implementations based on direct momentum injection (see Section 3.4). In these various models, the maximum momentum acquired by the parent molecular cloud is just L/c integrated over the lifetime of massive stars, namely

$$M_{\rm cl} v_{\rm rad} = \int \frac{L_{\rm rad}}{c}\mathrm{d}t = \frac{E_{\rm rad}}{c}, \quad (7)$$

where $E_{\rm rad} = \eta_{\rm SN} f_* M_{\rm cl} \epsilon_{\rm rad}$ and $\epsilon_{\rm rad} \simeq 10^{52}$ erg $\mathrm{M}_\odot^{-1}$ is the specific energy released in the form of radiation by massive stars. For the final cloud velocity acquired by radiation pressure due to a single scattering event, we obtain

$$v_{\rm rad} = \frac{1}{c}\frac{E_{\rm rad}}{M_{\rm cl}} \simeq 17\frac{\eta_{\rm SN}}{0.1}\frac{f_*}{0.1}\ \mathrm{km\,s^{-1}}. \quad (8)$$

Although the dependence on the star conversion efficiency and the IMF is stronger than in the blast wave case, we conclude from this analytical derivation that our radiation-driven energy-conserving model is generally much more efficient at converting radiation energy into gas momentum than radiation pressure from a single scattering event. Indeed, if all the radiation energy were to be absorbed in the cloud, we find $v_{\rm Sedov} \simeq 900\ \mathrm{km\,s^{-1}}$. This could be justified in the radiation-pressure picture by invoking a very high IR optical depth, corresponding to an unrealistic large ($\sim$45) number of multiple scattering events. Our energy-conserving approach should therefore be considered as a very optimistic model for radiation feedback. On the other hand, we are probably underestimating the gas density and the corresponding dust optical depth, because our spatial resolution is limited to 150 pc. Boosting artificially both the value of the dust opacity and the efficiency of radiation-pressure feedback could be considered as indirectly compensating for our limited resolution. The various optimistic factors we use in our implementation of radiation feedback can indeed be interpreted as a subgrid clumping factor on the effective dust opacity.

3.2 Numerical model for radiation feedback

Implementing a proper numerical model of radiation feedback is a formidable task. It requires modelling the absorption of UV radiation by dust, and its re-emission in the IR. The dust temperature has to be determined self-consistently using the energy balance between incident and re-emitted radiation. Proper radiative transfer of IR radiation through the dusty gas has then to be performed, using a dust opacity consistent with the computed dust temperature. This IR radiation will regulate the thermal state of the gas through

dust, but more importantly, it will transfer momentum to the gas through radiation pressure (Murray et al. 2010, 2011; Krumholz & Thompson 2012). This scenario is believed to be at work in GMCs, explaining why strong stellar feedback effects are observed (such as the apparent disruption of the GMC), although the stars are still too young to become SNe. It is beyond the scope of the paper to numerically model these very complex phenomena. We instead use a much simpler method to approximate the absorption of radiation by dust and the transfer of the re-emitted energy into gas momentum and strong outflows. The idea is to use the 'escape probability' model for stellar radiation. In each cell containing a young stellar particle reaching the age of 10 Myr, we assume that the UV radiation energy absorbed by the cell is given by

$$E_{\rm UV} = E_{\rm rad}\left[1 - \exp\left(-\kappa_{\rm UV}\rho_{\rm dust}\Delta x\right)\right]. \quad (9)$$

In the last equation, $E_{\rm rad} = 10^{52}$ erg $\mathrm{M}_\odot^{-1}$ is the total specific energy released during the first 10 Myr of a 10 $\mathrm{M}_\odot$ progenitor (see Fig. 1). The dust mass density is simply assumed to be equal to $\rho_{\rm dust} = Z\rho_{\rm gas}$, where Z is the mass fraction of metal ($Z = 0.02$ for a solar metallicity). The opacity used here is taken to be the dust opacity at 0.1 μm, namely $\kappa_{\rm UV} = 1000\,\mathrm{cm}^2\,\mathrm{g}^{-1}$ (Draine & Li 2007). We assume then that this UV radiation is immediately re-emitted in the IR band. The IR radiation energy absorbed by the same cell is also computed using the escape probability model

$$E_{\rm IR} = E_{\rm UV}\left[1 - \exp\left(-\kappa_{\rm IR}\rho_{\rm dust}\Delta x\right)\right], \quad (10)$$

where now $\kappa_{\rm IR}$ is the dust opacity in the appropriate IR band. This is the key parameter in our model, since it controls the amount of energy that will be given to the gas. We discuss how we model the IR dust opacity in the following section. The last remaining step is to transfer this IR energy into momentum in the gas. Many possibilities have been explored already in Hopkins, Quataert & Murray (2012), Stinson et al. (2012) and Agertz et al. (2013, see Section 3.4). We try to maximize the transfer of IR radiation energy into gas momentum by exploiting our existing SNe feedback model based on a slowly dissipative non-thermal energy component, and adding the absorbed IR radiation energy to the existing SNe energy. Since this additional non-thermal energy is basically conserved during $t_{\rm diss} = 10$ Myr, the transfer of IR energy into gas momentum during this period is maximized: we are in pure energy-conserving mode.

We now illustrate quantitatively the effect of radiation feedback in a single cell where a stellar particle releases both SNe energy and radiation energy (the latter being only partially absorbed using our escape probability model). Fig. 2 shows the total amount of radiative energy absorbed by the cell after reprocessing for a few representative values of $\kappa_{\rm IR}$. Note that very high densities and high opacities are required to funnel a significant fraction of the radiation energy into turbulent energy in this model. In Fig. 3, we have plotted the resulting specific energy of the non-thermal component for various values of the adopted IR dust opacity, as a function of the gas density. We assumed a cell size of $\Delta x = 200$ pc, solar metallicity and a Salpeter IMF. The dashed line shows the feedback energy for SNe alone, and the solid lines are the additional contribution from the absorbed IR radiation. One sees clearly in this plot that in high-density regions, the SNe energy will be severely diluted and the resulting gas velocity will never be able to reach the escape velocity of a MW-like halo ($v_{\rm esc} \simeq 700$ km s^{-1}, dashed line). Radiation feedback, on the other hand, will increase the specific energy enough to allow the gas velocity to stay above the escape velocity at much higher density. It is only at very high densities (in our example for $n_{\rm H} > 1000$ H cm^{-3}) that radiation feedback energy becomes eventually diluted enough to become inefficient. From this plot, we

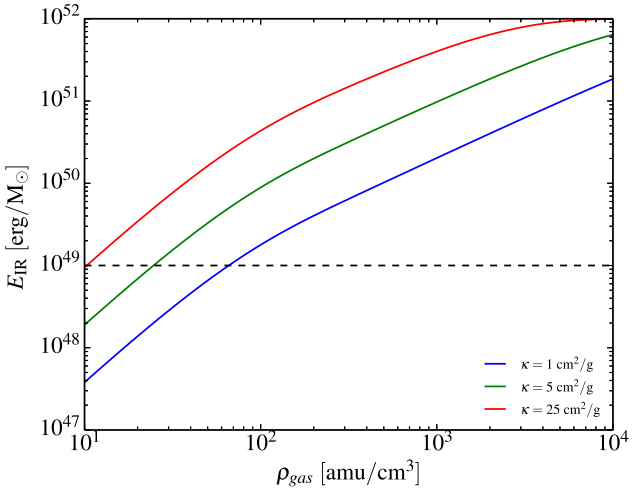

Figure 2. IR radiation energy absorbed by a cell (equation 10) for several representative values of $\kappa_{\rm IR}$, with $\Delta x = 200$ pc and $E_{\rm rad} = 10^{52}$ erg $\mathrm{M}_\odot^{-1}$. The dashed line shows the SN energy released per $\mathrm{M}_\odot$.

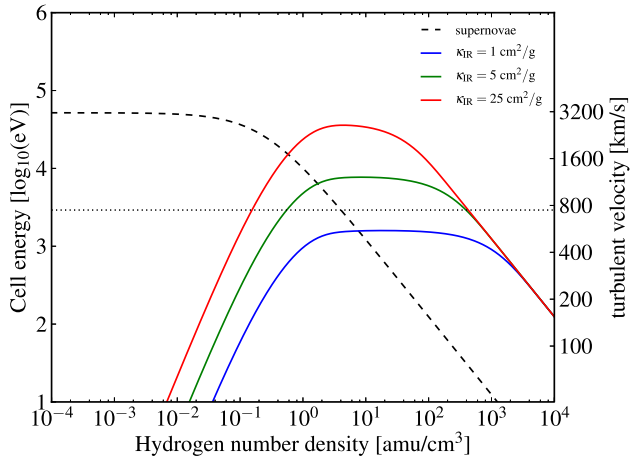

Figure 3. Non-thermal specific energy versus gas density, in a gas cell after a single star particle has released its SNe energy (dashed line), compared to the absorbed radiation energy (assuming solar metallicity and dust-to-metal ratio unity) for various values of the adopted dust opacity. The right-hand y-axis shows the resulting turbulent velocity. The dotted line shows the MW escape velocity (∼700 km s^{-1}) for comparison.

also see that the specific energy provided by radiation feedback will peak to a maximum value that depends directly on the adopted value for the dust opacity. For opacities lower than $\kappa_{\rm IR} < 1\,\mathrm{cm}^2\,\mathrm{g}^{-1}$, corresponding to cold dust with $T_{\rm dust} \simeq 10$ K, radiation feedback is never efficient enough to be able to raise the specific energy above the escape velocity of the MW. The regime $\kappa_{\rm IR} \simeq 5\,\mathrm{cm}^2\,\mathrm{g}^{-1}$ and above is however very interesting, because it allows the specific energy to stay significantly above the escape velocity and potentially provide a strong feedback mechanism. The correct value for the opacity depends crucially on the dust temperature, so we must provide a model for it.

3.3 Dust opacity model

We will adopt a pragmatic strategy, and first use the dust opacity (and the associated dust temperature) as a free parameter. The dust

Table 1. Simulation parameters.

Name	SN feedback	Metals	κ (cm^2 g^{-1})	var. κ
No feedback	n	n	n/a	n/a
SN only	y	y	0	n/a
$\kappa = 1-100$	y	y	1–100 (fixed)	n
var. κ	y	y	1–50 (variable)	y

opacity is a strong function of dust temperature with (Semenov et al. 2003)

$$\kappa_{\rm IR} \simeq 0.1 \left(\frac{T_{\rm dust}}{10\,{\rm K}}\right)^2 {\rm cm}^2\,{\rm g}^{-1}. \quad (11)$$

Using Wien's law for the typical wavelength for the IR radiation re-emitted by dust

$$\lambda_{\rm IR} \simeq 300 \left(\frac{T_{\rm dust}}{10\,{\rm K}}\right)^{-1} \mu{\rm m} \quad (12)$$

and dust opacity estimates from Draine & Li (2007), we deduce that temperatures of the order of $T_{\rm dust} \simeq 100$ K are required to raise the opacity to $\kappa_{\rm IR} \simeq 10$ cm^2 g^{-1}. In the simulation suite we present in this paper, we will explore values of the dust opacity varying between 1 and 100 cm^2 g^{-1} (see Table 1), corresponding to typical dust temperature ranging from 0 to 1000 K. The latter value is quite extreme, although it can be observed in active galactic nuclei (AGN) spectral energy distributions (SED), and is close to the limit of dust sublimation (Pier & Krolik 1992; Efstathiou & Rowan-Robinson 1995; Mullaney et al. 2011).

The main caveat of our adopted methodology is that dust temperature is a sensitive function of the environment (Desert, Boulanger & Puget 1990). A quiescent disc galaxy at redshift zero like the MW today will contain mostly cold dust with $T_{\rm dust} = 10$ K, except perhaps in some particularly actively star-forming region, where the dust temperature can reach $T_{\rm dust} = 30$ K. A strong nuclear starburst will provide enough UV radiation to significantly raise the cold dust temperature up to $T_{\rm dust} = 50$ K, and increase the contribution of a 'cool' dust component with $T_{\rm dust} = 150$ K (Marshall et al. 2007). Providing a self-consistent model for the dust temperature is beyond the scope of this paper. We will however use and explore a very simple model based on the local SFR as a proxy for the local UV radiation field. We assume that dust is in local thermodynamical equilibrium with the ambient radiation field, so that the dust temperature satisfies

$$\sigma T_{\rm dust}^4 = F_{\rm UV}, \quad (13)$$

where $F_{\rm UV}$ is the local UV radiation flux. We then assume that this radiation flux is proportional to the local SFR, which scales as $\dot{\rho}_* \propto \rho_{\rm gas}^{3/2}$, using a normalization factor consistent with typical MW conditions. This leads to the following very crude but physically motivated model for the dust temperature:

$$T_{\rm dust} = 10\,{\rm K} \left(\frac{\rho_{\rm gas}}{0.1\,{\rm H\,cm^{-3}}}\right)^{3/8}, \quad (14)$$

which is used in equation (11) to compute the local dust IR opacity. We have checked that this model is consistent with dust temperature in the range 30–50 K, in good agreement with IR galaxies SED (Marshall et al. 2007). In what follows, we call this opacity model the 'varying κ' model, as opposed to the other simpler models where $\kappa_{\rm IR}$ is fixed during the course of the simulation (see Table 1).

3.4 Comparison to other models

Radiation-pressure feedback has only recently been considered in numerical work studying the formation and evolution of galactic discs (e.g. Hopkins et al. 2011, 2012; Wise et al. 2012; Agertz et al. 2013; Aumer et al. 2013; Stinson et al. 2013b). It is therefore useful to discuss how these studies differ from the one presented here.

In the suite of papers by Hopkins et al., an implementation of radiation-pressure feedback was explored using SPH, relying on high mass ($m_{\rm SPH} \sim 10^3\,{\rm M}_\odot$) and force resolution ($\sim$ few pc). Here radiation pressure was modelled as direct injection of momentum into the local ISM at the rate

$$\dot{p}_{\rm rad} \approx (1 + \tau_{\rm IR}) \frac{L(t)}{c}, \quad (15)$$

where $L(t)$ is the luminosity of the considered stellar population, and $\tau_{\rm IR}$ the IR optical depth through the surrounding dense star-forming gas. The first (order unity) term in the above equation describes the direct absorption/scattering of photons from gas or dust. Hopkins et al. adopted an on-the-fly Friends-of-Friends (FOF) technique to locate star-forming clouds and calculate the local gas surface density $\Sigma_{\rm cl}$, hence directly modelling $\tau_{\rm IR} \approx \kappa_{\rm IR}\,\Sigma_{\rm cl}$. Here $\kappa_{\rm IR}$ is scaled with the local gas metallicity to allow for varying dust-to-gas ratios. In this model, radiation feedback was shown to affect SF properties in galaxies from dwarfs to extreme starbursts, where the contribution was most significant in the systems with a high surface density.

Agertz et al. (2013) explored a purely local subgrid implementation of radiation pressure suitable for high-resolution cosmological simulations ($\Delta x < 100$ pc). Momentum injection was modelled via equation (15), where $\tau_{\rm IR}$ was calculated via an empirical model based on the observed size–mass relation of molecular clumps and young star clusters. Dust photon trapping was here only assumed to operate at very early ($t < 3$ Myr), embedded stages of star cluster formation.

Aumer et al. (2013) took a similar approach in their SPH simulations, but considered a large fixed value of the IR optical depth, $\tau_{\rm IR} = 25$. To allow for a more gentle momentum input in low-redshift systems, the authors scale $\tau_{\rm IR}$ with a factor $(\sigma_{\rm gas}/40\,{\rm km\,s^{-1}})^3$, where $\sigma_{\rm gas}$ is the local gas velocity dispersion. In contrast to Agertz et al. (2013), the momentum boost from IR photon trapping is assumed to operate at all times.

Wise et al. (2012) demonstrated, using an AMR radiative transfer technique, how radiation pressure in the single scattering regime (i.e. $\tau_{\rm IR} = 0$) could affect SFRs and the metal distribution in dwarf galaxies situated in dark matter haloes of mass $2 \times 10^8\,{\rm M}_\odot$. This work is one of the few self-consistent treatments of momentum feedback from radiation in galaxy formation simulations, but due to the large computational expense involved this approach is not yet widely used.

All of the above (subgrid) work consider radiative feedback as direct injection of *momentum* into the ISM, over various time-scales, whereas we consider radiative feedback by injecting the absorbed radiation *energy* into a separate feedback energy variable, which in turn generates momentum. Along similar lines, Brook et al. (2012) and Stinson et al. (2013b) discussed the importance of 'early feedback' in their SPH galaxy formation simulations. These authors assume that 10 per cent of the *bolometric* luminosity radiated by young stars gets converted into thermal energy, which significantly affected properties of their simulated galaxies. In contrast to our model, no consideration was taken with regards to modelling the actual absorbed radiation energy via local dust UV and IR absorption (equations 9 and 10).

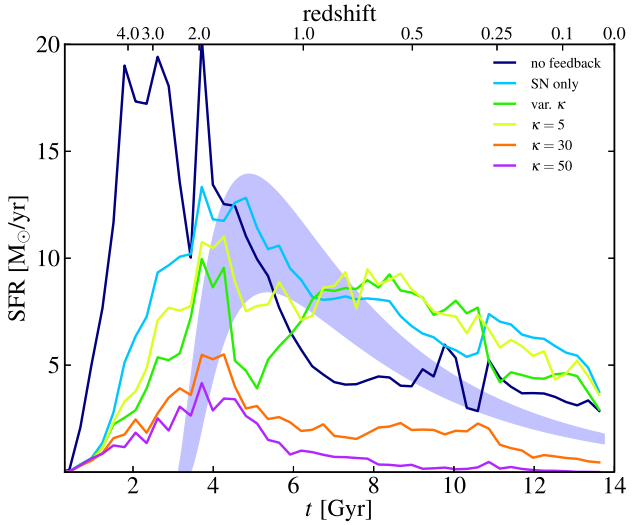

Figure 4. SFHs for stars found within 20 kpc of the centre at $z = 0$. The shaded blue area shows the SFR for $10.4 < \log(M_*/\mathrm{M}_\odot) < 10.6$ from Leitner (2012).

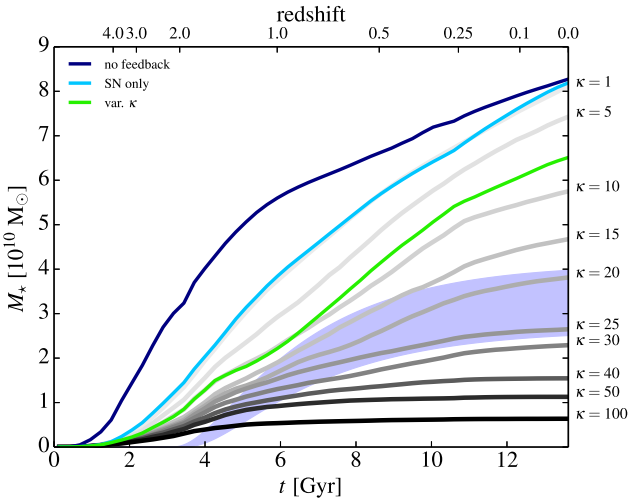

Figure 5. Cumulative stellar mass as a function of time. Grey-scale lines represent runs with different fixed values of κ, as indicated by the values on the right-hand side of the figure. The blue shaded region shows the data from Leitner (2012).

Ultimately, subgrid implementations of radiation pressure must be compared on the basis of how much momentum is generated in a single SF event as a function of environment, and to what extent this drives galactic scale outflows. As we have shown in Section 3.1, our implementation very efficiently converts the available energy into gas momentum via radiation pressure.

4 RESULTS

Here, we describe the basic outcomes of our radiative feedback simulations. We begin by discussing the effects of radiative feedback on baryonic mass assembly, followed in later sections with increasingly detailed diagnostics of final gas and stellar properties, disc structure and the IGM.

4.1 SF histories

Recently, a great deal of effort has been made in cosmological galaxy formation simulations to suppress efficient SF at high redshifts. When the early SFR is stifled, the formation of massive stellar spheroids is halted in their infancy (Agertz et al. 2011; Brook et al. 2011). One method that has been shown to work well in SPH-based schemes is based on limiting the 'sites' of SF to only the highest density regions (Governato et al. 2010). The result is that SF is highly localized, resulting in a more vigorous injection of SN energy into the surrounding ISM. This enables the SN feedback to more efficiently modulate the SFR, thereby suppressing the formation of star-heavy protogalaxies and preserving the gas for the formation of extended structures later in the evolution.

The simulations in our suite resolve structures down to $\Delta x_{\rm min} \simeq 160$ pc, and the stars form in gas cells with densities above the resolvable density limit of $\rho_{\rm J} \simeq 2.4$ H cm^{-3} (see Section 2.3). In Fig. 4, we show the star formation histories (SFHs) for all of the runs in the suite. The SN-only run shows that even in the absence of radiative feedback, our SN feedback scheme is efficient at shifting the bulk of SF to a later time and somewhat lowering its peak.

The inclusion of radiative feedback affects the star-forming regions much more drastically than the SN feedback alone, which is apparent in the further suppression of high-z SF. The var. κ and $\kappa = 5$ runs come close to the observational relations (the shaded blue area shows the observationally constrained SFH from Leitner 2012), until $z \sim 0.5$. At lower redshifts, the SFRs are elevated due to the previously expelled material re-accreting to the centre, where the potential well is now deep enough to prevent permanent expulsion. The two higher κ cases are much too efficient at shutting down SF after $z \sim 1.5$. Note that we show the Leitner (2012) data for a range of stellar masses. These correspond to the expected stellar mass given our halo mass and the SMHM relation from Moster, Naab & White (2013).

In Fig. 5, we show the cumulative mass assembly history of the stars found in our central galaxy at $z = 0$. The latter is defined as the entire region within $0.1 r_{200}$. Coloured lines show the no-feedback, SN-only and var. κ runs, while the grey lines show the various fixed-κ runs. The shades of grey correspond to the opacity values shown in the colour bar, while the blue shaded region shows the results from Leitner (2012). The immediate impact of radiative feedback on the production efficiency of stars is evident, especially at early times. The SN feedback alone results in factor 2 fewer stars by $z = 2$, though because the gas is not successfully ejected from the halo it can be recycled and the overall stellar mass of the $\kappa = 0$ run at $z = 0$ is nearly identical to the run without any feedback at all. Increasing amounts of radiative feedback facilitate the expulsion of more baryons, thus resulting in an overall decrease in the amount of stars formed. Importantly, the assembly time (defined as the moment when half of the stellar mass is in place) is shifted to later times, in principle allowing for a more extended stellar structure to form.

4.2 SMHM relation

The statistical SMHM relation (e.g. Conroy & Wechsler 2009; Behroozi, Wechsler & Conroy 2013; Moster et al. 2013) links the observed stellar mass content of galaxies to theoretical dark matter halo masses. It therefore provides a crucial check on the baryonic physics included in simulations and specifically on the resulting efficiency of feedback mechanisms.

In Fig. 6, we show the ratio of stellar mass to halo mass (SMHM) as a function of halo mass for the runs in our suite. The dashed black line and the grey area show the mean relation and the 1σ error from

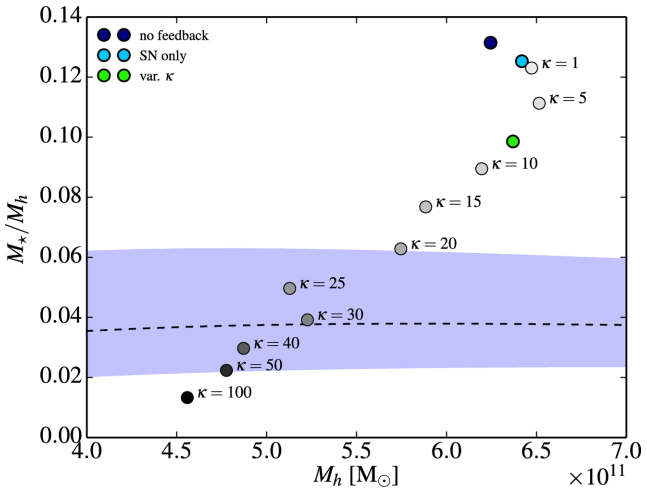

Figure 6. Stellar mass versus halo mass for all the simulations in the suite. The stellar and halo masses are measured at $0.1r_{200}$ and r_{200}, respectively. The black dashed line shows the mean of the abundance-matching relation from Moster et al. (2013) with the shaded area showing the extent of the errors. Grey dots represent the runs with fixed values of κ, as indicated by the colour bar.

Moster et al. (2013). Once again, we show the selected runs with coloured points and the remaining fixed-κ runs in different shades of grey. κ must be increased to >20 in order to fall within the 1σ relation. Note that although the no-feedback and SN-only runs have nearly identical stellar masses, their points are offset in the SMHM relation due to a 5 per cent difference in the dark matter and gas mass.

We emphasize that the relation from Moster et al. (2013) should be taken only as a reference point; we have simulated only a single halo, which may well lie on the fringe of the population due to its specific formation history. Determining whether these results are independent of the assumed merger history is beyond the scope of this paper, but will be addressed in a future work. On the other hand, some authors have cautioned that the seeming disagreement between simulated and observed stellar masses may stem from inherent biases in inferring stellar masses in observational surveys (Munshi et al. 2013). In this paper, we report the theoretical values in order to study the qualitative effects of feedback on the process of galaxy formation and do not try to mimic observational techniques.

An interesting feature of Fig. 6 is that increasing feedback efficiency only leads to a monotonic decrease in the stellar mass fraction and halo mass after a certain threshold. $M_{\rm h}$ actually *increases* from the no-feedback case until $\kappa = 5$. The reason for the increasing $M_{\rm h}$ is that while the stellar mass is steadily decreasing, the mass of the gas retained in the halo actually increases appreciably, deepening the potential well and therefore also increasing the halo dark matter mass within r_{200} due to adiabatic contraction. The increase in gas mass is due to two effects. First, with increased feedback the metal fraction in the halo increases, enabling more efficient cooling of halo gas and partially counteracting the effect of the winds launched from the disc. With even stronger feedback, the SF quenching is strong enough to prevent significant metal production therefore reducing the metal-induced cooling in the halo, in addition to driving a more vigorous wind, again reducing the halo gas mass. We discuss the metallicity in the halo further in Section 4.3. Secondly, the relatively cold gas that is launched from the disc mixes with the coronal gas, boosting the ability of halo gas to cool and remain bound (e.g. Marinacci et al. 2010). Together, these two effects lead to a 50 per cent increase in halo gas mass with $\kappa = 5$ over the no-feedback case. The gas mass remains higher than the no-feedback case for $\kappa < 20$.

4.3 IGM and gas recycling

As hinted by Fig. 6, the increased energy budget provided by radiation feedback has an important effect on the properties of halo gas. Figs 7 and 8 show colour maps representing temperature, density and metallicity by red, green and blue colours, respectively. Red regions represent hot, low-density gas, green/brown regions are low-metallicity dense gas, and cyan regions represent dense, metal enriched gas. The colour scheme highlights the qualitative differences in the effect of various feedback schemes on the medium surrounding the central galaxy.

In Fig. 7, we see that all of the radiative feedback models produce energetic, metal-enriched outflows, despite the differences in their SFRs. One exception is the $\kappa = 5$ case, which successfully reduces the SFR (see Fig. 4), but does not provide enough energy to drive an efficient outflow. The SN-only case shows that even at high redshift the metals are largely remaining locked inside the central object. Radiative feedback is also very efficiently heating the surrounding IGM, resulting in a much larger hot corona already at a $z = 2$.

Fig. 8 illustrates the qualitative present-day IGM differences induced by feedback-driven winds. In the case without radiative feedback, essentially all metals are locked entirely within the central object, with only a hint of metal pollution in the circum-galactic medium (CGM). On the other hand, the radiative feedback drives large, halo-scale fountains that successfully transport metals even beyond the virial radius. However, at $\kappa > 30$, the SFR is reduced to the point of substantially reducing the overall halo metal mass fraction. In the $\kappa = 50$ case, the metallicity of the halo is low relative to the other radiative feedback runs and there is very little gas recycling taking place between the disc and the halo.

In the remaining two fixed κ cases, we see that the 'fountain' reaches well beyond r_{200}, which measures ∼175 kpc (decreasing by ∼10 per cent for high-κ runs). The variable κ run on the other hand results in a smaller fountain and is enriching the halo but not expelling the gas completely. This helps retain a higher SFR at late times. In Fig. 8, we also see a substantial amount of mixing taking place between the hot and cold phase, which lowers the overall temperature of the corona and allows the gas to cool more efficiently and return to the disc (see also the above discussion of Fig. 6). The top panel of Fig. 9 shows the quantitative differences in mean halo gas temperatures as a function of feedback strength. Paradoxically, stronger feedback actually leads to a *cooler* gas halo owing to the gas mixing and increased cooling due to a higher metal mass fraction (bottom panel of Fig. 9).

The metal budget of the CGM provides an important constraint on the SF and feedback processes that take place throughout a galaxy's lifetime. Recently, observations of QSO sightlines that intersect the haloes of nearby galaxies have been used to provide estimates on the column densities of various ions (e.g. Prochaska et al. 2011; Tumlinson et al. 2011; Werk et al. 2013). In particular, the high abundance of O IV has been used to argue that additional energetic feedback, beyond SNe, is required in models of galaxy formation to yield the requisite metal mass fractions in galactic haloes (Stinson et al. 2012; Hummels et al. 2013).

The bottom panel of Fig. 9 shows the estimated column density of O VI in our models. We derive the O VI mass fraction in each cell by obtaining the O VI ionization fraction from CLOUDY (Ver. 10, Ferland et al. 2013) given the temperature and density of each

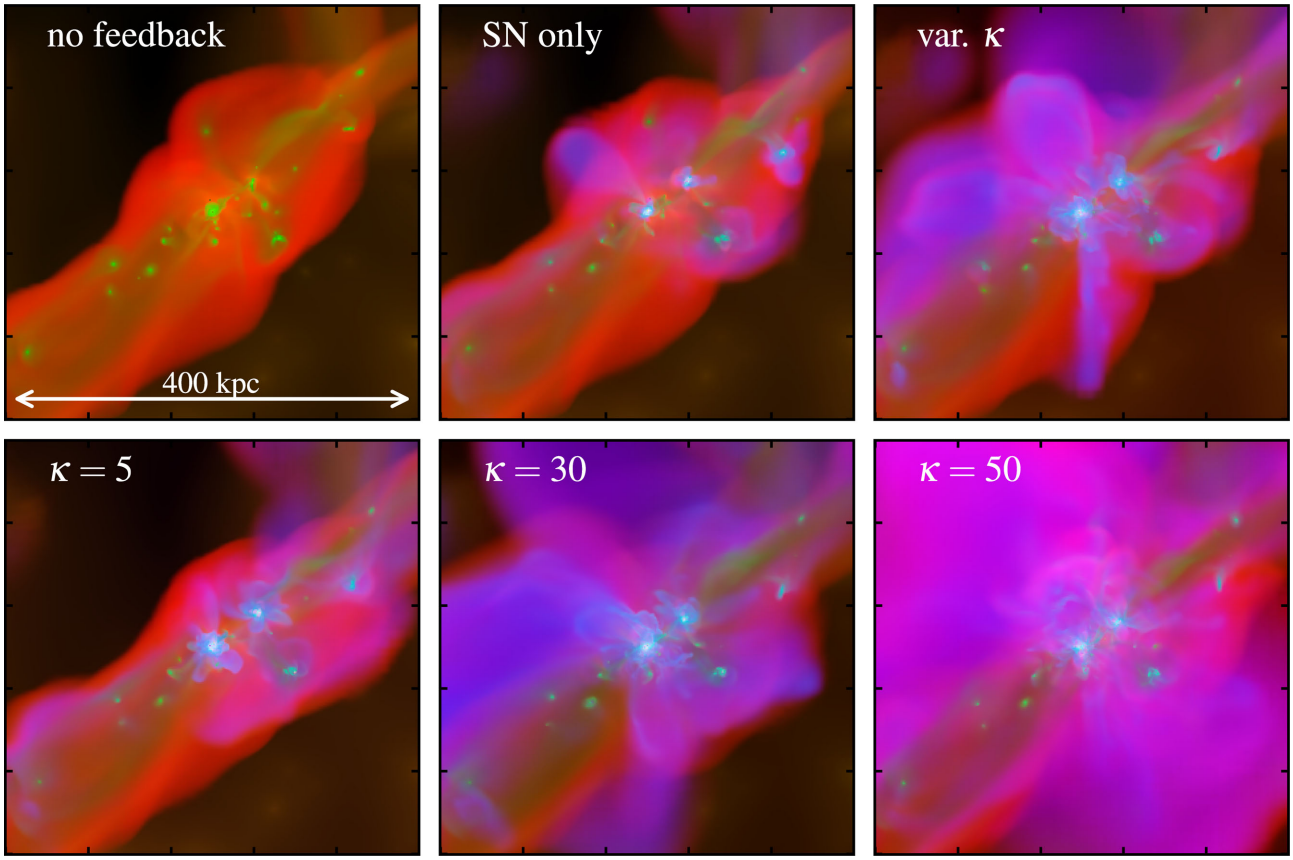

Figure 7. Mass-weighted temperature/density/metallicity maps shown in projection at $z = 2$. Red, green and blue colours represent temperature, density and metallicity, respectively. The boxes used for the projections are 400 kpc on a side.

cell. We estimate the O VI mass fraction in each cell by scaling the metallicity to the solar value of oxygen abundance and multiplying it by the O VI fraction. Our estimates are crude and meant to serve as qualitative indicators of metal pollution in the galactic halo as a function of different feedback strengths. Accurately deriving O VI mass fractions in cosmological simulations is complicated by the fact that at our resolution we do not adequately resolve the small-scale structure of the IGM to account for ionization state variations which depend sensitively on local cloud properties. This is particularly true for O VI since the ionization fraction varies by several orders of magnitude within a narrow temperature range (Tumlinson et al. 2011).

With these caveats in mind, our order-of-magnitude estimates illustrate the importance of an efficient feedback mechanism for reaching the requisite metal column densities in the IGM. In the case of SN-only feedback, the O VI fraction is too low by 2–3 orders of magnitude, due to the combination of too few metals expelled into the halo and a very high halo temperature. Radiative feedback at even modest ($\kappa = 5$) levels boosts the halo metal fraction by two orders of magnitude. Interestingly, relatively strong feedback ($\kappa \sim 30$) is required to produce a flat O VI profile in the outer parts of the halo. However, *too much* feedback decreases the IGM metal fraction, owing to a low SFR. The IGM metal profiles therefore restrict the range of κ to ∼20–30, similar to the abundance matching constraints discussed in Section 4.2, though none of the models match the observations at 100 kpc particularly well.

We have also considered whether the assumed dust opacities could significantly affect the SEDs of our galaxies, thereby further constraining the appropriate choice of κ. Estimates of the dust optical depth $\tau_{\rm dust} = \int \rho_{\rm dust}(s)\kappa {\rm d}s$, where s is the path taken along the line of sight, yield a maximum value of 0.05 in the edge-on orientation for the $\kappa = 20$ case at $z = 0$. The $\kappa = 5-20$ range yields a maximum in $\tau_{\rm dust}$ since it allows for reasonably high densities but also produces a significant amount of metals (see Fig. 9). At higher κ values, the increased opacity cannot compensate for the reduction in metals. Nevertheless, we find that throughout the range of opacities we consider the dust remains optically thin and we therefore do not expect that it should drastically affect the disc SED.

4.4 Morphology, kinematics and structural properties

Given the efficient coupling of the strong radiative feedback to the ISM, it must consequently also have an effect on the morphology of the resulting discs. A successful model of a galaxy at this mass should not only yield a system that matches observations in its physical characteristics, but it should also appear morphologically consistent with what we know of late-type spiral galaxies. In Scannapieco et al. (2012), for example, the only galaxies with flat rotation curves and satisfying the observational SMHM relation from the Aquila comparison project (G3-TO, R-AGN and G3-BH) are all spheroid-dominated at $z = 0$. Furthermore, fully cosmological models rarely yield discs with clearly-defined spiral structure in both gas and stars.

In Fig. 10, we show the face-on and edge-on density-weighted gas densities for all the runs in our suite. It is evident that the inclusion of radiative feedback even at lower fixed κ produces a highly disturbed

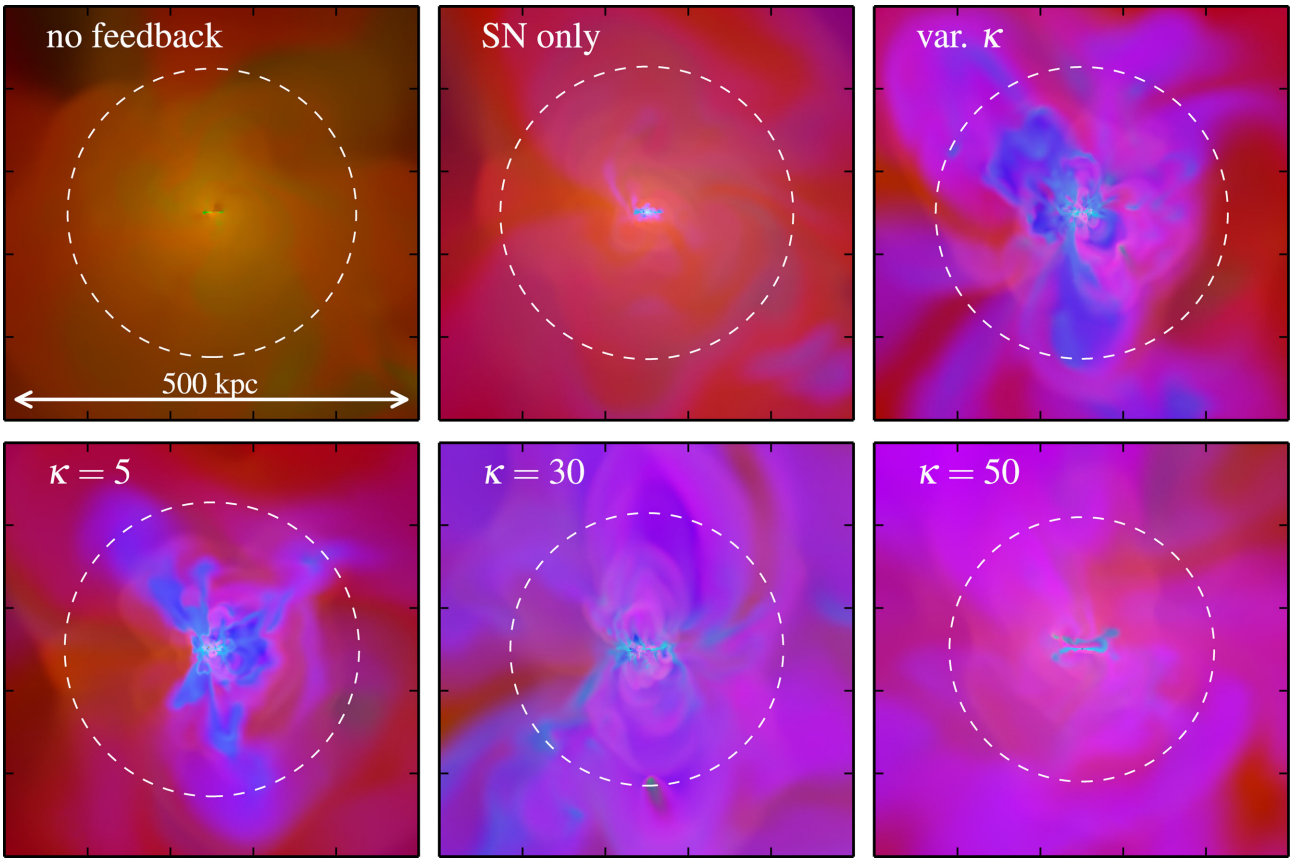

Figure 8. Slices of the gas distribution at $z = 0$. The colour scheme is the same as in Fig. 7. The system is aligned such that the disc is seen edge-on. r_{200}, indicated by dashed white circles, are ∼175 kpc except in the $\kappa = 30$ and $\kappa = 50$ runs where they are 10 per cent smaller. The boxes used for the slices are 500 kpc on a side.

morphology. On the other hand, the no-feedback and SN-only runs produce much more ordered discs with well-defined spiral arms. Interestingly, the $\kappa = 50$ case yields an impressively 'quiet' disc at $z = 0$, with only a few knots of SF visible. The strong feedback expels enough gas from the disc region that the present-day SFRs are essentially zero. At $\kappa = 30$, enough gas survives in the halo to continually drive SF and consequently large-scale winds. Fig. 6 above shows that only relatively high values of κ push the models towards the abundance matching values of SMHM relation, placing an opposite constraint on the feedback efficiency.

Fig. 10 shows only the gas component, but the stellar properties are also significantly affected. Fig. 11 shows mock images of the stars and highlights the drastic change in the morphology as a function of feedback strength. All of the radiative feedback runs lack a thin star-forming component, and apart from the no-feedback run hardly any large-scale spiral structure appears. The stellar component thickens with the disc fraction noticeably reduced. In Fig. 12, we quantify the stellar properties further, showing the stellar surface densities (Σ_*), the rotation curves ($v_{\rm circ}$), $V_{\rm rot}/\sigma$ and the $z_{\rm rms} \equiv \sqrt{\overline{z^2}}$, where z is the position of particles perpendicular to the disc plane. The latter quantity is used as a model-independent measure of disc thickness. We scale the x-axis by the scalelength of each system, obtained by performing a maximum likelihood fit to a radially exponential disc with a sech^2 vertical profile (using EMCEE; Foreman-Mackey et al. 2013; see Roškar, Debattista & Loebman 2013; Stinson et al. 2013a). The fits yield scalelengths, $R_{\rm d}$ of 2.1 and 3.3 kpc for the no-feedback and SN-only runs, respectively, while the var. κ, $\kappa = 5$, $\kappa = 30$ and $\kappa = 50$ runs have scalelengths of 4.5, 4.5, 4.9 and 3.6 kpc, respectively. In order to isolate only the stars near the centre, only particles within a cylinder 10 kpc thick are used. The results are not sensitive to any reasonable choice of this selection criterion.

The inclusion of *any* of our feedback mechanisms (even the SN-only case) results in a drastic reduction of the stellar bulge, extends the disc and flattens the rotation curve. The effect of feedback on disc structure is most evident in the two right-hand panels of Fig. 12. For the majority of runs with feedback, the overall $V_{\rm rot}/\sigma < 3$ in the disc region. The dashed lines show the relation for stars formed less than 3 Gyr ago. The no-feedback run shows strong rotational support in the young component, while the other runs have poor rotational except in the outer parts of the disc. In the MW, by comparison, young and old stars near the solar circle (at $\sim 3R_{\rm d}$) have $V_{\rm rot}/\sigma \sim 10$ and ∼4, respectively (these are shown with dashed and dotted black lines in the third panel). While the structures in our simulations with feedback have some rotational support, they are clearly far from forming thin discs. This is similar to an earlier result by Governato et al. (2007), who found that increasing the SN feedback efficiency significantly affected their disc morphologies. Interestingly, the $\kappa = 50$ run produces a fairly thin young disc, but the SFR is so low that it fails to contribute significantly to the mass.

The disc thickness, quantified in the rightmost panel (and qualitatively seen in Fig. 11), also increases as a function of κ. Typical late-type discs have $z_{\rm rms} \sim 1$ kpc. In the MW, young (old) stars have scaleheights of 200–300 pc (∼900 pc; Bovy et al. 2012). The

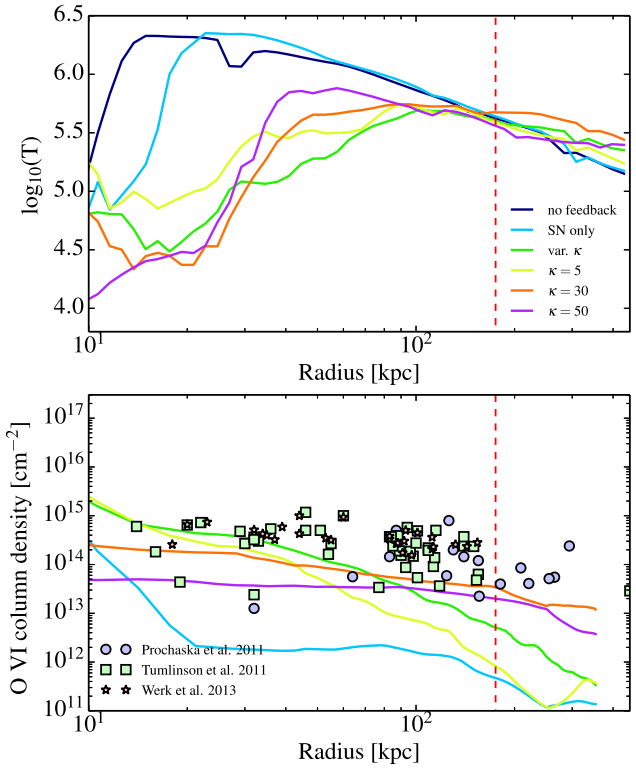

Figure 9. Mean halo gas temperature (top) and column density of O VI as a function of radius (bottom) at $z = 0$. See text for details regarding the O VI estimate. The vertical dashed line shows the location of the virial radius.

thinnest disc is formed by the no-feedback run, though it is also the most concentrated and strongly flared. Again, in the rightmost panel we use all stars to measure the $z_{\rm rms}$. If we use only young stars instead, the no-feedback $z_{\rm rms}$ is ∼100 pc, while for other runs it is only about a factor of 2 lower, indicating that in the other runs even the young stars comprise a relatively thick component.

As suggested by Fig. 12, the disordered nature of the discs manifests itself most clearly in the kinematic properties of the stars. Fig. 13 shows the eccentricity parameter defined as $\epsilon = j_z/j_{\rm c}(E)$, where j_z is the z-component of the angular momentum of the star and $j_{\rm c}(E)$ is the angular momentum of a star in a circular orbit with the same energy. The calculation of $j_{\rm c}(E)$ is only strictly valid in the mid-plane and since in some of the runs a significant fraction of stars are away from the plane this results in $j_z/j_{\rm c} > 1$ values. Note also that this definition of 'circularity' is different than what is used sometimes in the literature, where j_z is compared to the angular momentum of stars on circular orbits *at the same radius* (e.g. Scannapieco et al. 2012). Fig. 13 shows that increasing κ reduces the rotationally supported fraction (identified by $\epsilon \sim 1$), i.e. the feedback in part exacerbates a problem it was meant to resolve in the first place. The variable κ run, although very efficient at reducing the SFR at early times, approaches the kinematics of the SN-only and low-κ cases owing to the reduced feedback efficiency at late times.

Suppressing early SF is believed to also help with reducing the bulge-to-total (B/T) ratio of disc systems that form in cosmological simulations. Observationally, the majority (70 per cent) of observed late-type spirals with $M_* > 10^{10}\,M_\odot$ have B/T ratios <0.2. On the other hand, even the most successful state-of-the-art simulations

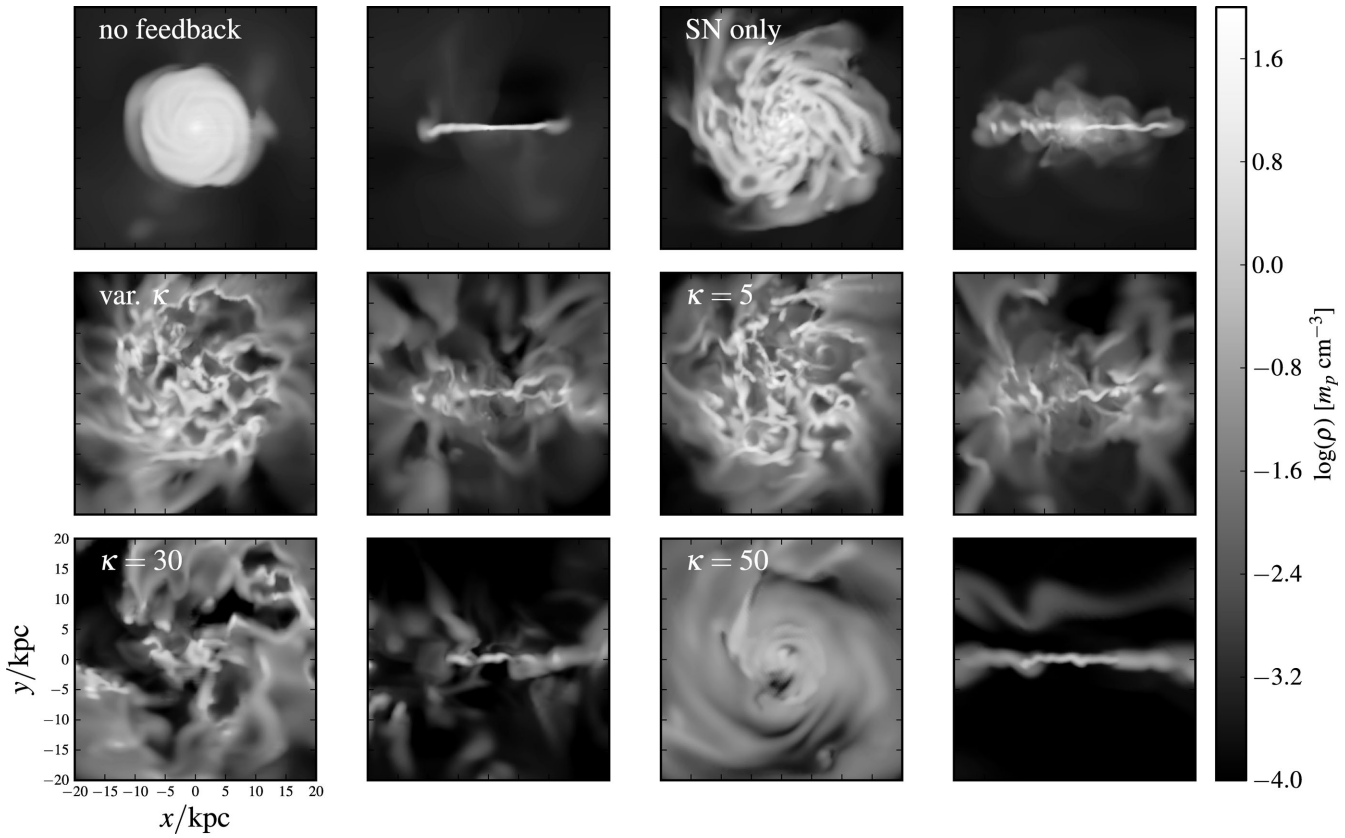

Figure 10. Face-on and edge-on slices showing the structure of gas discs at $z = 0$. None of the radiative feedback runs (middle and bottom rows) show clearly defined spiral structure, and all feedback processes significantly deform the discs.

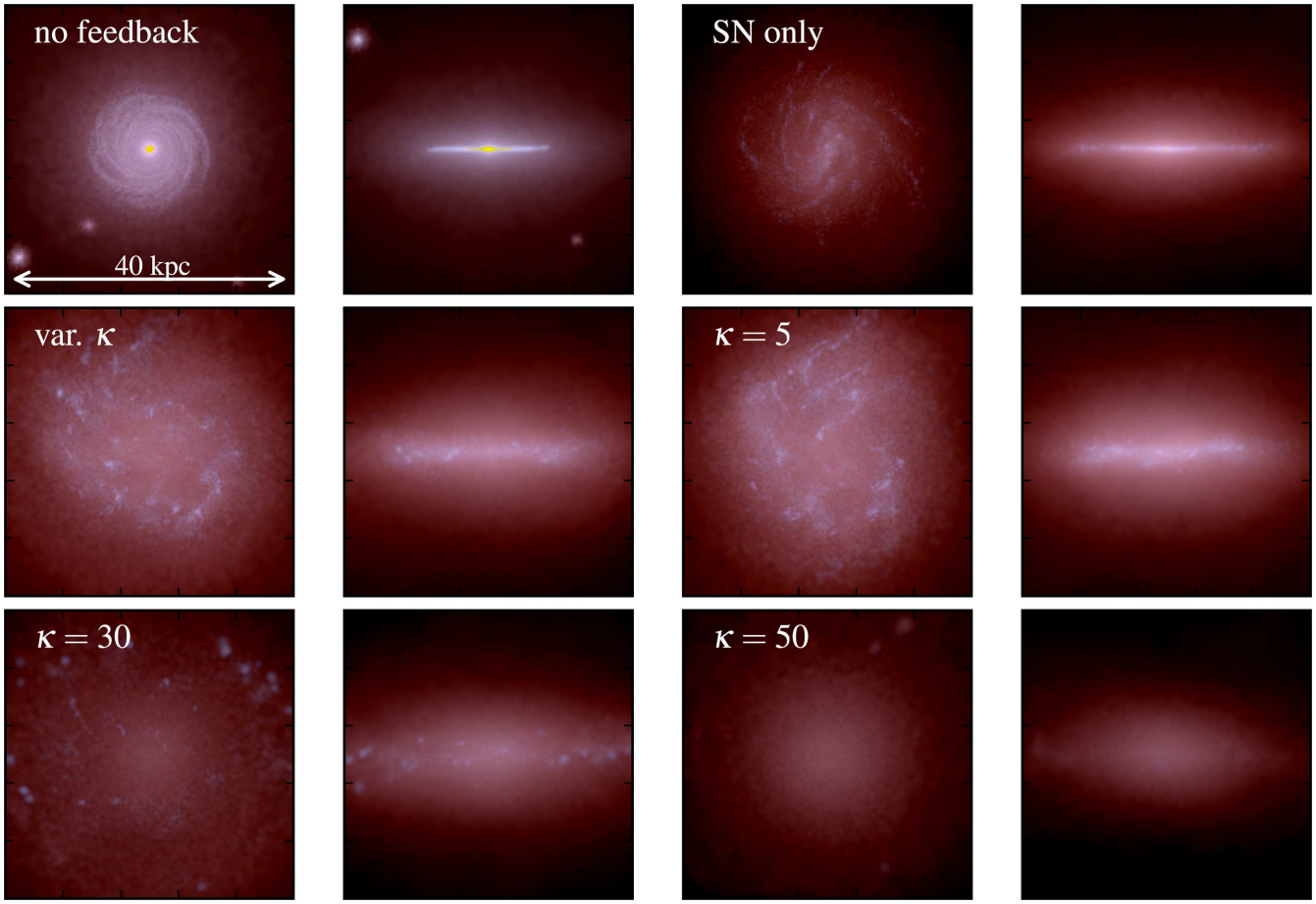

Figure 11. Composite colour images of the stars at $z = 0$ constructed by using the K, B and U magnitude maps as the R, G and B image channels, respectively. The magnitudes are calculated using the Padova Simple stellar populations (SSPs) from Marigo et al. (2008).

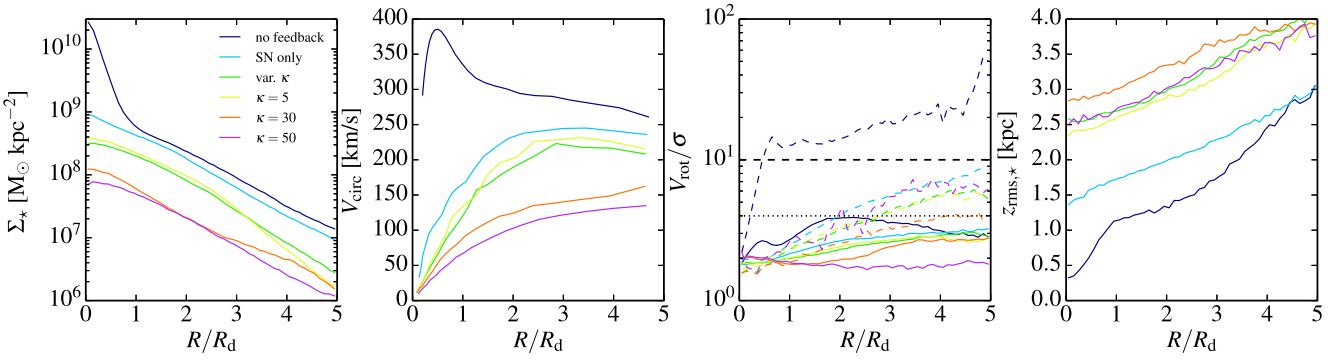

Figure 12. Radial profiles for all the simulations in the suite at $z = 0$. From left to right, the panels are showing: stellar surface density Σ_*; the circular velocity $v_{\rm circ}$; the ratio of mean stellar tangential velocity $V_{\rm rot}$ and stellar velocity dispersion σ; the $z_{\rm rms}$, where z is the particle vertical position with respect to the disc mid-plane, as a model-independent proxy for the thickness of the stellar distribution. In the third panel, the solid lines are calculated using all particles, while we only use stars younger than 3 Gyr for the dashed lines. The black dashed and dotted lines are showing the $V_{\rm rot}/\sigma$ for MW young and old stars, respectively.

(e.g. the *Eris* simulation) form systems with B/T > 0.2. Leitner (2012) stress that delaying SF in late-type systems until $z < 2$ is critical for resolving this issue, and indeed this seems to have been the case in both SPH-based simulations (Brook et al. 2011) and AMR-based simulations (Agertz et al. 2011). While our $\kappa = 0$ run shows only a minor shift in the formation time, the radiative feedback models successfully attenuate the early $z > 2$ SF (Fig. 4). However, the same process (radiative feedback) that shifts the bulk of SF towards late times, contributes directly to the formation of the kinematically hot component. Paradoxically, the run without *any* feedback yields the most rotationally supported disc structure and a comparatively low fraction of its stars are trapped in the low angular momentum component. Note that this finding is seemingly in contradiction to most previous investigations (with the exception of the AMR simulations in Agertz et al. 2011 based on a low SFE $\epsilon_* \simeq 0.01$), which typically find that feedback is needed to create

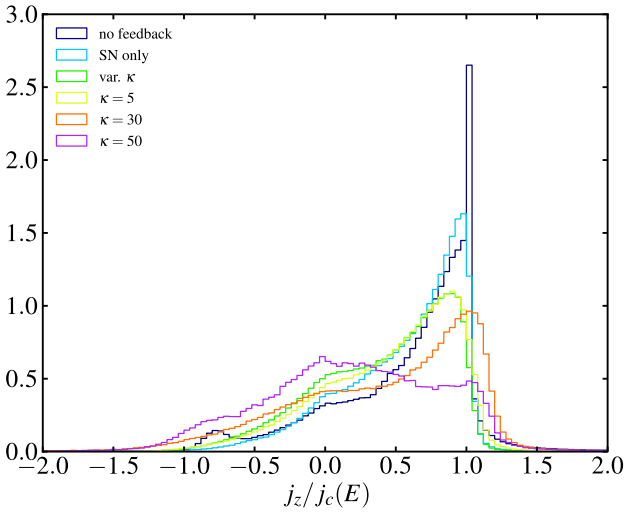

Figure 13. Histograms of the ratio of angular momentum to maximum angular momentum at the star's energy, $j_z/j_c(E)$ at $z = 0$. Each histogram is normalized so that the area integral is unity.

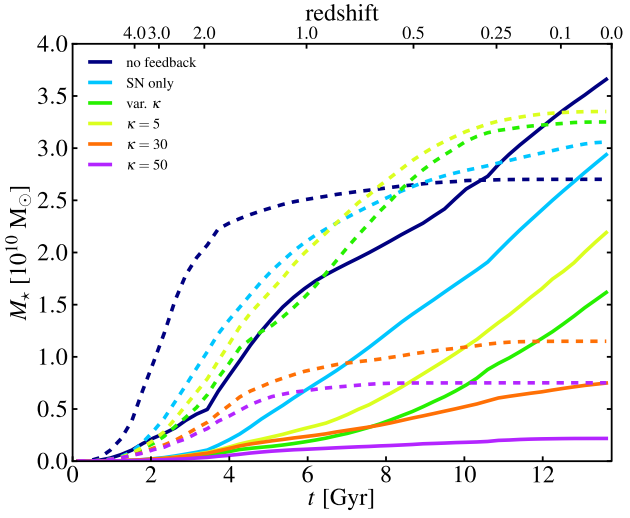

Figure 14. Cumulative mass assembly as a function of time for $\epsilon = j_z/j_c(E) > 0.8$ (i.e. disc stars, solid lines) and $\epsilon < 0.5$ (spheroid stars, dashed lines).

a system with a reasonable disc mass fraction. We stress here that it is critical to make a distinction between 'bulge' and 'spheroid'; moderate amounts of feedback (even SN feedback alone) are plenty to remove the bulge, but increasing the feedback further results in a stronger and extended high-dispersion component instead of a thin disc.

In light of this, we examine how the velocity dispersion- and rotation-dominated components grow. In Fig. 14, we show the cumulative stellar mass formation history for stars found within 20 kpc of the main halo centre, subdivided by their circularity, ϵ. The evolution of the mass fractions of the two components is somewhat counterintuitive. First, modest feedback models (SN only and low κ) confirm the results from the literature (e.g. Brook et al. 2011) and delay the formation of the bulge. However, at the same time feedback *enables* the formation of an extended spheroid at late times, by sufficiently stirring the gas component and preventing a quiescent disc from forming. We see in Fig. 14 that for this particularly simple separation of disc and spheroid stars, the no-feedback case is the only one that forms a disc-dominated system. This follows from the previous work of Agertz et al. (2011), who showed a degeneracy between efficient feedback and inefficient SF. Nevertheless, the SN-only and low-κ cases successfully reduce the bulge fraction (stars forming before $z \sim 2$), but boost the overall spheroid fraction. In this case, the low-ϵ stars are not comprising the bulge (as is frequently assumed) but instead form an extended spheroidal component. They would not be detected as bulge-like in a photometric disc/bulge decomposition, as can also be seen from the left-hand panel of Fig. 12, and would likely yield a low B/T ratio. It is clear from the rightmost panel of Fig. 12 that these systems are much too thick and too dispersion-dominated to be considered late-type disc-like.

5 CAVEATS IN OUR MODELLING APPROACH

5.1 Radiation feedback model

In our radiative feedback model described in Section 3.2, we try to capture some of the essential aspects of the interaction between radiation from massive stars and the surrounding ISM. Naturally, because the model is 'subgrid', many caveats are inherently present.

The major caveat in any scheme implementing 'radiative' feedback is that its proper treatment requires costly radiative transfer calculations. In the absence of such a detailed radiative transfer implementation, we opted for a simple radiation budget prescription that involves the major physically relevant parameters (dust opacity to UV and IR radiation). Our simplified prescription (equations 9 and 10) uses the cell size to compute the column density of typical star-forming region. Since our minimum cell size is 160 pc, the optical depth of star-forming regions is certainly poorly approximated. It is not clear, however, what would be the effect of increasing the resolution. Higher resolution will lead to smaller cell sizes, but also higher densities. The column density of dust will probably increase, leading to a stronger effect of radiation feedback. On the other hand, in intermediate density regions, the smaller cell size will lead to smaller opacities and radiation might escape too easily. A proper treatment of radiation transport might be required to avoid this. This effect of numerical resolution could be alleviated using a clumping factor approach: the average opacity inside a coarse cell can be modified by the underlying, unresolved density fluctuations. Again, the effect is unclear: although clumpiness will boost the effect of radiation pressure on dense clouds, the presence of underdense regions will allow radiation to escape more efficiently.

As discussed in the methods section, we do not include a radiation-pressure model for momentum transfer between the stellar radiation and the ISM. Instead, we simply combine the energy obtained by equation (10) in the overall energy budget deposited in the region that is affected by stellar feedback. We use a non-thermal energy variable (associated with cosmic rays, magnetic fields or turbulence) that slowly decays over a fixed dissipation time-scale of 10 Myr. This non-thermal energy variable is used to determine whether the flow remains adiabatic or whether cooling is restored. The qualitative effect of this model, very similar to the Stinson et al. blast wave model, is to maximize momentum injection in the gas from the available feedback energy. As we have shown in this paper, this allowed us to explore very strong feedback scenarios and analyse the properties of the resulting galaxy. Although this model does not claim to be a fully consistent physical model of stellar feedback,

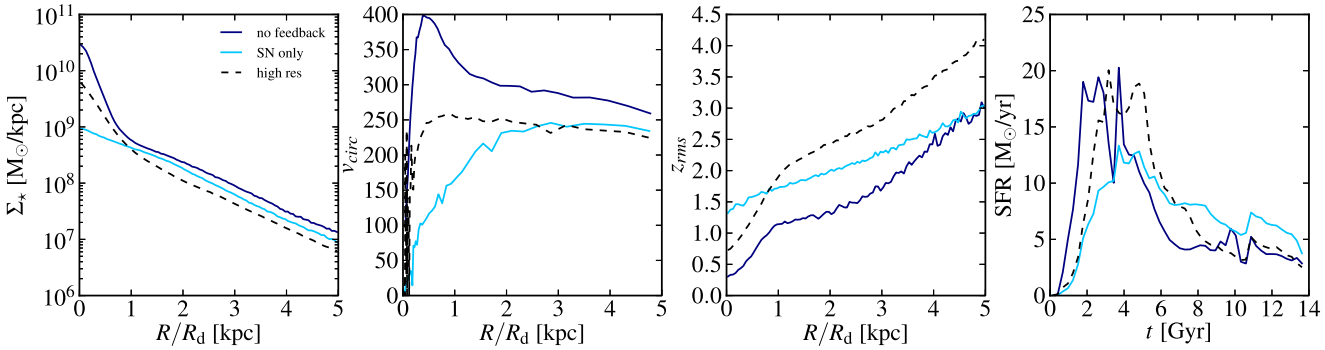

Figure 15. Comparison of the no-feedback and SN-only runs to the higher-resolution simulation using the SN-only feedback prescription (dark blue, light blue and dashed lines, respectively). From left to right: stellar surface density, rotation curve, $z_{\rm rms}$ and SFR.

it allows us to maximally exploit the available energy provided by stellar feedback.

5.2 SF gas density threshold

Our choice of subgrid parameters, especially the density threshold for SF, affects the locations of SF. Because increasing feedback efficiency thickens the gas disc, the density threshold parameter in principle also controls the scaleheight of newly formed stars if gas above the plane of the disc exceeds the threshold. In recent years, boosting the SF threshold has become a popular method for creating extended thin discs, but we stress here that we are not free to choose an arbitrarily high threshold. Subgrid SF prescriptions should take over from the self-consistent hydrodynamical modelling when the gas exceeds the dynamic range of the simulation (see Section 2.3). Therefore, at these resolutions, the use of a higher density threshold is unphysical.

Nevertheless, we conducted additional experiments to assess the sensitivity of disc properties on the threshold parameter. We ran additional simulations with $\rho_\star = 24\,{\rm H\,cm^{-3}}$ (i.e. 10 times our fiducial threshold) with $\kappa = 1$ and $\kappa = 5$. The simulations confirmed the notion stated already many times in the literature that increasing the SF threshold results in a burstier SFR, effectively concentrating the feedback energy into more isolated events. Our $\kappa = 5$ ($\kappa = 1$) run therefore behaved similarly to $\kappa \sim 25$ ($\kappa = 5$) in terms of abundance matching. Structurally, the simulations yielded a thinner gas disc but the disc stellar mass fraction remained low compared to the spheroid. We therefore conclude that although there seems to be a degeneracy between adopted subgrid parameters controlling the locations of SF and feedback efficiency, our fiducial choices do not artificially boost the disc to spheroid fraction.

5.3 Simulation resolution

One last caveat of our numerical models is the limited resolution and its impact on gas dynamics. The fact that our simulated gas discs appear to be strongly perturbed by feedback could be attributed to excessive numerical diffusion, leading to excessive momentum mixing between the cold, star-forming clouds and the warm, wind-blown gas in the corona. Since increasing the resolution will lead to a reduced numerical diffusion in the momentum equation, we expect the coupling between the cold disc and the turbulent fountain to weaken. On the other hand, if turbulent diffusion is the main process leading to mixing within the disc, then the increased resolution will not reduce the mixing. Furthermore, as with any subgrid feedback scheme, one must worry that the chosen set of parameters may not translate well on to a simulation with different resolution.

In Fig. 15, we compare the fiducial no-feedback and SN-only runs to a higher-resolution simulation using the SN-only feedback model. The higher resolution run uses eight times more particles, a spatial resolution of $\sim$100 pc and a SF threshold of $\sim 10\,{\rm H\,cm^{-3}}$. The SN feedback affects the gross disc structure less in the higher resolution run, presumably due to slightly reduced mixing efficiency when the disc structure becomes better resolved. This results in weaker suppression of SF, especially at early times, as evident by the increased bulge fraction and elevated SFR at early times. Nevertheless, the feedback is efficient enough to prevent the formation of an unreasonably dense bulge, resulting in a much flatter rotation curve compared to the no-feedback run.

Our primary motivation for this comparison is to determine whether the under-resolved disc structure causes the feedback to have a disproportionate effect on the ISM. At higher resolution the feedback energy might be distributed on smaller scales, preventing the efficient destruction of disc structure apparent in Fig. 10. This effect, coupled with the higher threshold for SF, could lead to a thinner disc thereby partially alleviating our worries about the incompatibility of strong feedback and reasonable disc morphology.

The third panel of Fig. 15 shows, however, that the high-resolution disc is not appreciably thinner than the no-feedback and SN-only cases at our fiducial resolution. There is a notable decrease in disc thickness in the centre owing to current vigorous SF there, but the remainder of the disc is actually thicker than in the lower resolution case. We attribute this to the fact that the higher SF threshold leads to more vigorous local energy injection (e.g. Governato et al. 2010), boosting the overall efficiency of feedback. This is similar to the effect we described above in runs at fiducial resolution but with a higher ρ_*. In addition, we also checked that the angular momentum distribution, V/σ, and the halo metal profiles did not change considerably. We therefore conclude that it is not immediately clear that higher resolution should resolve some of the problems with strong feedback outlined previously.

A further caveat related to resolution is that the maximum allowed grid refinement level is increased at pre-determined epochs (see Section 2). Each time the refinement is increased, the gas may settle quickly to reach higher densities than before. This can lead to formation of spurious dense structures, increasing the SFR and consequently resulting in stronger feedback potentially influencing the disc thickness shown in Fig. 12. While we cannot rule out that this effect is taking place, we see no obvious spikes in the SFR that should occur if the effect was significant (see Fig. 4, redshifts

4, 1.25 and 0.25). This is also confirmed by visual inspection of outputs before and sufficiently after the refinement level change.

6 DISCUSSION AND SUMMARY

In the preceding sections, we argued that disagreement between the simulated and observed stellar mass fractions motivates the inclusion of additional baryonic feedback processes. We further demonstrated the need for additional feedback in Section 3.1 by showing that for a MW-sized halo, SN feedback alone does not provide enough energy to unbind the gas from the system. On the other hand, radiation from young massive stars is a source of energy roughly two orders of magnitude larger than that of SNe alone. As a result, this source of energy has been shown in the recent literature to be quite successful in regulating the stellar mass fraction and bring systems simulated in the full cosmological context closer to observations (Brook et al. 2012; Stinson et al. 2013b).

Marinacci, Pakmor & Springel (2014) have argued that such exotic feedback schemes are not necessary, and presented models in which SN-only feedback yields stellar mass fractions consistent with abundance matching estimates and morphologically regular discs. Their feedback model incorporates only SNe, but it produces an artificially decoupled wind (Vogelsberger et al. 2013) whose velocity is scaled according to the escape velocity of the host halo (see also Springel & Hernquist 2003; Oppenheimer & Davé 2008). Such a velocity scaling, although empirically motivated, ensures that some of the gas is unbound from the halo. They therefore do not require 'tricks' in modelling the gas component such as shutting off cooling to mimic a blast wave (e.g. Stinson et al. 2006). It is not clear, however, that endowing the wind with the escape velocity is any more natural or physical than other tricks used to more strongly couple the subgrid prescriptions to the state of the gas.

The goal of all energetic feedback prescriptions is to remove gas from its host halo and prevent the formation of excessively concentrated stellar components as well as to control the stellar mass fraction. We have shown in the preceding sections that while radiation feedback can certainly provide the required energy to produce a large-scale galactic wind, it is essentially *impossible* to simultaneously produce a morphologically undisturbed thin disc. The only way that one can preserve a kinematically cool disc in which to form a quiescent stellar component is to somehow prevent the gas affected by feedback from mixing with the surrounding ISM. In the case of feedback implementations in SPH codes, mixing is weakened due to the well-known inability of SPH to accurately resolve the instabilities that should arise in such a scenario (Agertz et al. 2007). We speculate that this numerical effect makes it somewhat easier to impart large amounts of energy on to the gas locally while at the same time leaving the larger scale structure of the disc unaffected even at relatively coarse resolutions of several hundred pc. On the other hand, when the winds are explicitly decoupled from the rest of the flow (e.g. Aumer et al. 2013; Marinacci et al. 2014; Puchwein & Springel 2013; Vogelsberger et al. 2013) they do not significantly affect the disc component by construction. Instead, they may efficiently find their way to the outer halo or even escape the host completely leaving behind an unperturbed disc.

To summarize, despite the ability of modern simulation codes to capture an impressive dynamic range, hydrodynamic simulations of MW-like galaxies forming in the cosmological context require the use of analytic prescriptions to capture unresolved physics on the smallest scales. In particular, SF and the coupling of stellar feedback to the surrounding gas depends heavily on such subgrid models. Using the AMR code RAMSES, we have explored the effects of stellar radiation feedback on the evolution of MW-like discs.

Our suite of simulations confirms earlier results that radiation feedback efficiently reduces the stellar mass fraction by providing sufficient energy and momentum to permanently expel gas from the host halo. However, our experiments have also revealed a previously underappreciated conundrum: if the feedback is strongly coupled to the local ISM, it becomes impossible to satisfy the stellar mass fraction constraints without simultaneously destroying the disc morphology. In fact, while increasing the feedback efficiency serves to reduce the bulge and the overall stellar mass fraction, it also significantly boosts the kinematically warm spheroidal component. Our results also highlight the importance of energetic feedback beyond SN driven winds to sufficiently pollute the IGM with metals. The metal enrichment and expulsion of warm gas to large galactocentric distances further enhances the mixing in the IGM. As a result, increasing feedback efficiency up to a certain point paradoxically results in enhanced retention of gas within the virial radius. We therefore conclude that while transporting gas from the disc region into the IGM and beyond the virial radius appears to be a necessary component of galaxy formation, it is unclear at present how this can be achieved without sacrificing the disc morphology in the process. The efficiency of gas mixing within the multiphase turbulent ISM and IGM appears as the key factor in regulating the disc morphology and the metal distribution within the halo.

ACKNOWLEDGEMENTS

We thank the anonymous referee for a very constructive report. Simulations were performed on the Monte Rosa and the Piz Daint systems at the Swiss Supercomputing Center (CSCS) and the local supercomputer *Z*box3 at the Institute for Theoretical Physics, University of Zürich. RR was supported by a University of Zürich Forschungskredit grant and the Marie Curie Career Integration Grant. RT and MW were supported by the Swiss National Science Foundation through the HP2C programme. We thank Greg Stinson, Chris Brook and Lucio Mayer for comments on an earlier draft of this manuscript. We gratefully acknowledge fruitful discussions with Claude-Andre Faucher-Guigueres, Elliot Quaetert, Davide Elbaz, Emeric LeFloc'h. We also thank Sam Leitner for providing us with his SFH and cumulative stellar mass data.

REFERENCES

Abadi M. G., Navarro J. F., Steinmetz M., Eke V. R., 2003, ApJ, 597, 21
Agertz O. et al., 2007, MNRAS, 380, 963
Agertz O., Teyssier R., Moore B., 2011, MNRAS, 410, 1391
Agertz O., Kravtsov A. V., Leitner S. N., Gnedin N. Y., 2013, ApJ, 770, 25
Aumer M., White S. D. M., Naab T., Scannapieco C., 2013, MNRAS, 434, 3142
Bastian N., Goodwin S. P., 2006, MNRAS, 369, L9
Behroozi P. S., Wechsler R. H., Conroy C., 2013, ApJ, 770, 57
Bournaud F., Elmegreen B. G., Teyssier R., Block D. L., Puerari I., 2010, MNRAS, 409, 1088
Bovy J., Rix H.-W., Liu C., Hogg D. W., Beers T. C., Lee Y. S., 2012, ApJ, 753, 148
Brook C. B. et al., 2011, MNRAS, 415, 1051
Brook C. B., Stinson G., Gibson B. K., Wadsley J., Quinn T., 2012, MNRAS, 424, 1275
Chabrier G., 2001, ApJ, 554, 1274
Conroy C., Wechsler R. H., 2009, ApJ, 696, 620
Vecchia Dalla C., Schaye J., 2012, MNRAS, 426, 140
Desert F.-X., Boulanger F., Puget J. L., 1990, A&A, 237, 215

Draine B. T., Li A., 2007, ApJ, 657, 810
Efstathiou A., Rowan-Robinson M., 1995, MNRAS, 273, 649
Eisenstein D. J., Hut P., 1998, ApJ, 498, 137
Ferland G. J. et al., 2013, Rev. Mex. Astron. Astrofis., 49, 137
Foreman-Mackey D., Hogg D. W., Lang D., Goodman J., 2013, PASP, 125, 306
Fromang S., Hennebelle P., Teyssier R., 2006, A&A, 457, 371
Governato F. et al., 2004, ApJ, 607, 688
Governato F., Willman B., Mayer L., Brooks A., Stinson G., Valenzuela O., Wadsley J., Quinn T., 2007, MNRAS, 374, 1479
Governato F. et al., 2010, Nature, 463, 203
Guedes J., Callegari S., Madau P., Mayer L., 2011, ApJ, 742, 76
Guillet T., Teyssier R., 2011, JCoPh, 230, 4756
Haardt F., Madau P., 1996, ApJ, 461, 20
Hopkins P. F., Quataert E., Murray N., 2011, MNRAS, 417, 950
Hopkins P. F., Quataert E., Murray N., 2012, MNRAS, 421, 3488
Hummels C. B., Bryan G. L., Smith B. D., Turk M. J., 2013, MNRAS, 430, 1548
Katz N., Weinberg D. H., Hernquist L., 1996, ApJS, 105, 19
Knollmann S. R., Knebe A., 2009, ApJS, 182, 608
Kravtsov A. V., Klypin A. A., Khokhlov A. M., 1997, ApJS, 111, 73
Krumholz M. R., Tan J. C., 2007, ApJ, 654, 304
Krumholz M. R., Thompson T. A., 2012, ApJ, 760, 155
Krumholz M. R., McKee C. F., Tumlinson J., 2009, ApJ, 699, 850
Leitherer C. et al., 1999, ApJS, 123, 3
Leitner S. N., 2012, ApJ, 745, 149
Marigo P., Girardi L., Bressan A., Groenewegen M. A. T., Silva L., Granato G. L., 2008, A&A, 482, 883
Marinacci F., Binney J., Fraternali F., Nipoti C., Ciotti L., Londrillo P., 2010, MNRAS, 404, 1464
Marinacci F., Pakmor R., Springel V., 2014, MNRAS, 437, 1750
Marshall J. A., Herter T. L., Armus L., Charmandaris V., Spoon H. W. W., Bernard-Salas J., Houck J. R., 2007, ApJ, 670, 129
Moore B., Ghigna S., Governato F., Lake G., Quinn T., Stadel J., Tozzi P., 1999, ApJ, 524, L19
Moster B. P., Somerville R. S., Maulbetsch C., van den Bosch F. C., Macciò A. V., Naab T., Oser L., 2010, ApJ, 710, 903
Moster B. P., Naab T., White S. D. M., 2013, MNRAS, 428, 3121
Mullaney J. R., Alexander D. M., Goulding A. D., Hickox R. C., 2011, MNRAS, 414, 1082
Munshi F. et al., 2013, ApJ, 766, 56
Murray N., Quataert E., Thompson T. A., 2010, ApJ, 709, 191
Murray N., Ménard B., Thompson T. A., 2011, ApJ, 735, 66
Navarro J. F., Steinmetz M., 1997, ApJ, 478, 13
Navarro J. F., Steinmetz M., 2000, ApJ, 538, 477
Navarro J. F., White S. D. M., 1994, MNRAS, 267, 401
Navarro J. F., Frenk C. S., White S. D. M., 1997, ApJ, 490, 493
Oppenheimer B. D., Davé R., 2008, MNRAS, 387, 577
Pérez F., Granger B. E., 2007, Comput. Sci. Eng., 9, 21
Pier E. A., Krolik J. H., 1992, ApJ, 401, 99
Pontzen A., Governato F., 2012, MNRAS, 421, 3464
Pontzen A., Roškar R., Stinson G., Woods R., 2013, pynbody: N-Body/SPH analysis for python, ascl:1305.002
Prochaska J. X., Weiner B., Chen H.-W., Mulchaey J., Cooksey K., 2011, ApJ, 740, 91
Puchwein E., Springel V., 2013, MNRAS, 428, 2966
Rasera Y., Teyssier R., 2006, A&A, 445, 1
Roškar R., Debattista V. P., Loebman S. R., 2013, MNRAS, 433, 976
Scannapieco C. et al., 2012, MNRAS, 423, 1726
Semenov D., Henning T., Helling C., Ilgner M., Sedlmayr E., 2003, A&A, 410, 611
Springel V., Hernquist L., 2003, MNRAS, 339, 289
Springel V., Frenk C. S., White S. D. M., 2006, Nature, 440, 1137
Steinmetz M., Muller E., 1995, MNRAS, 276, 549
Stinson G., Seth A., Katz N., Wadsley J., Governato F., Quinn T., 2006, MNRAS, 373, 1074
Stinson G. S. et al., 2012, MNRAS, 425, 1270
Stinson G. S. et al., 2013a, MNRAS, 436, 625
Stinson G. S., Brook C., Macciò A. V., Wadsley J., Quinn T. R., Couchman H. M. P., 2013b, MNRAS, 428, 129
Teyssier R., 2002, A&A, 385, 337
Teyssier R., Chapon D., Bournaud F., 2010, ApJ, 720, L149
Teyssier R., Pontzen A., Dubois Y., Read J. I., 2013, MNRAS, 429, 3068
Truelove J. K., Klein R. I., McKee C. F., Holliman J. H., II, Howell L. H., Greenough J. A., 1997, ApJ, 489, L179
Tully R. B., Fisher J. R., 1977, A&A, 54, 661
Tumlinson J. et al., 2011, Science, 334, 948
Vogelsberger M., Genel S., Sijacki D., Torrey P., Springel V., Hernquist L., 2013, MNRAS, 436, 3031
Werk J. K., Prochaska J. X., Thom C., Tumlinson J., Tripp T. M., O'Meara J. M., Peeples M. S., 2013, ApJS, 204, 17
White S. D. M., Rees M. J., 1978, MNRAS, 183, 341
Wise J. H., Abel T., Turk M. J., Norman M. L., Smith B. D., 2012, MNRAS, 427, 311

This paper has been typeset from a TEX/LATEX file prepared by the author.